

1 **Bidirectional bedform fields at the head of a**
2 **submarine canyon (NE Atlantic).**

3
4
5 Claudio Lo Iacono^{1,2*}, Jorge Guillen¹, Queralt Guerrero¹, Ruth Duran¹, Catherine
6 Wardell², Rob Hall³, Tahmeena Aslam³, Gareth Carter⁴, Jenny Gales⁵, Veerle A.I.
7 Huvenne²

8 ¹ *Marine Sciences Institute, Spanish National Research Council, Paseo Marítimo de la*
9 *Barceloneta 37-49, 08003 Barcelona, Spain*

10 ² *National Oceanography Centre, University of Southampton, Waterfront Campus,*
11 *Southampton, United Kingdom*

12 ³ *Centre for Ocean and Atmospheric Sciences, School of Environmental Sciences,*
13 *University of East Anglia, Norwich Research Park, Norwich, United Kingdom*

14 ⁴ *British Geological Survey, The Lyell Centre, Research Avenue South, Edinburgh, United*
15 *Kingdom*

16 ⁵ *University of Plymouth, School of Biological and Marine Sciences, Drake Circus,*
17 *Plymouth, PL4 8AA, United Kingdom*

18
19 *: corresponding author. E-mail address: loiacono@icm.csic.es

20
21 **ABSTRACT**

22 Submarine canyons are known to force ocean mesoscale circulation and local
23 hydrodynamics. Alternate up- and down-canyon near-bottom flows have been widely
24 documented along the upper reaches, connecting the canyon heads with the contiguous
25 outer shelves and vice versa. Nonetheless, we still miss clear evidence of bedform fields
26 expressing these complex patterns. In this study, through a multi-scale analysis in both
27 space and time, we document rare asymmetric bedforms, up to 880 m long and 10 m
28 high, developing within a depth range of 168-220 m at the head of the Whittard Canyon
29 (NE Atlantic). One field of well-developed sandwaves has an atypical up-slope
30 asymmetry, with the steeper slope facing the shallower regions of the shelf, and

31 contrasting with surrounding down-slope sandwaves facing the canyon. The bedforms
32 are interpreted to represent both up-slope and down-slope bottom currents connecting
33 the upper reaches of the canyon to the outer shelf on the southern Celtic Margin, in the
34 Bay of Biscay. The sandwaves were surveyed with shipboard Multibeam bathymetry (5
35 m grid cell resolution), AUV sidescan sonar (0.15 m grid cell resolution) and ROV
36 footage, and sampled with three ROV-mounted vibro-cores and two box-cores.
37 Sidescan sonar mosaics groundtruthed by ROV footage and sediment samples show
38 with unprecedented detail spectacular trains of fresh overprinting megaripples,
39 previously undocumented sand peaks and bowl-shaped depressions on the crests of the
40 tallest sandwaves. Differences in sedimentary settings and benthic habitats indicate that
41 these features are currently active in particularly dynamic areas, allowing for very slow
42 migration of sandwaves. Modelling of the internal tide regime together with concurrent
43 hydrographic observations suggest large-amplitude semi-diurnal internal tides, possibly
44 transitioning to asymmetric internal bores, as the main mechanism maintaining the
45 mapped up-slope sandwaves. This work highlights the importance of uncommon
46 sediment dynamics in canyon head environments and adds insight to the traditional
47 notions of gravity-driven processes, being dominant in these environments, envisaging
48 implications for improving geo-hazard assessment of mobile substrates and
49 quantification of offshore sediment and carbon fluxes.

50

51 **Keywords:** Bedforms, seafloor mapping, marine robotics, geomorphology, submarine
52 canyons, internal tides

53 **1. INTRODUCTION**

54 The increasing detail of high-resolution mapping of bedform fields across several
55 continental shelves around the world is regularly revealing uncommon morphological

56 patterns related to complex and variable sedimentary and hydrodynamic regimes. For
57 example, observations on coastal and inner shelf settings report sandwave fields
58 migrating in opposite directions related to intricate hydrodynamic patterns (Van
59 Landeghem et al., 2012; Jiang and Lin, 2016). The dynamics of these bedforms are
60 generally controlled by the interplay of storm-forced currents and steered residual tidal
61 flows, acting over a variable local geomorphology (Boe et al., 2009; Van Landeghem et
62 al., 2012).

63 However, present-day activity of bedforms on sediment-starved outer shelf settings,
64 deeper than 100 m and far from modern fluvial sediment inputs, is still poorly
65 understood, mainly due to the lack of detailed seafloor mapping and long-term
66 hydrodynamic observations. In these settings, which are less sensitive to coastal
67 hydrodynamics and storm-induced flows, sandwave dynamics are mainly related to
68 along-shelf geostrophic circulation, generally reactivating relict sandy deposits
69 developed during previous sea-level stages (Lo Iacono et al, 2010; Rovere et al., 2019).

70 These hydrodynamic patterns can become more complex in the vicinity of shelf-incising
71 submarine canyons (Allen and Durrieu de Madron, 2009; Li et al., 2019). The upper
72 reaches of canyons are major conduits for down-slope gravitational flows funnelling
73 sediments to the deep-sea (Piper and Normark, 2009; Paull et al., 2011; Azpiroz-Zabala
74 et al., 2017), and may also promote up- and down-slope sediment transport related to
75 amplified internal waves (Allen and Durrieu de Madron, 2009; Puig et al., 2013; Li et
76 al., 2019). However, we are still missing clearly documented evidence of bedform field
77 migration in relation to such hydrodynamic processes, connecting the canyon head to
78 the shallower adjacent shelf and vice versa. Yet, these findings may have relevant
79 implications in ensuring the long-term integrity of offshore infrastructures (e.g. wind-
80 farm foundations, subsea pipelines, and tele-communication cables) close to mobile

81 substrates, in addition to better defining the patterns of organic and oxygen rich fluxes
82 across continental margins (Ahmerkamp et al., 2015). During the JC125 CODEMAP
83 Cruise, aimed to map and quantify complex deep-sea habitats of the Whittard Canyon
84 (NE Atlantic), we used a combination of routine and advanced marine robotic
85 technologies (shipboard / Autonomous Underwater Vehicle (AUV) mapping, Remotely
86 Operated Vehicle (ROV)-mounted vibro-cores, box-cores, ROV footage), to document
87 atypical bedform fields, mapped on the Celtic outer shelf between 168 and 220 m water
88 depth, showing contrasting geomorphological patterns at the head of the eastern canyon
89 branch (Fig. 1). We: 1) describe the morphology and sedimentology of different
90 superimposed bedforms, 2) examine the role of the Whittard Canyon in their generation
91 and evolution, with specific reference to internal tides, and 3) discuss their long- and
92 short-term dynamics.

93 **2. GEOLOGICAL AND OCEANOGRAPHIC SETTING**

94 The Celtic margin is a passive continental margin that extends WNW-ESE between the
95 Goban Spur and the Berthois Spur (Bourillet et al., 2006, Fig. 1). The continental shelf,
96 connected with the English Channel, is up to 500 km wide and connects with a steep
97 structurally controlled continental slope (average 8°). The geomorphology of the shelf is
98 irregular, with around 45 linear sand ridges, 40 to 180 km long, crossing the shelf
99 roughly perpendicular to the continental slope between 100 m and 200 m water depth
100 (Bouysse et al., 1976; Praeg et al., 2015) (Fig. 1a). These ridges correspond to
101 glacial sand banks formed between 20 and 12 ka BP (Pantin and Evans, 1984;
102 Scourse et al., 2009) and have been partially reworked by tidal flows during the last
103 marine transgression (Berné et al., 1998; Reynaud et al., 1999). The Whittard Canyon,
104 200 km long, is the largest of several submarine canyons incising the Celtic margin
105 (Mulder et al., 2012; Amaro et al., 2016). It extends from the shelf-edge, 200 m deep, to

106 the base of the continental slope, 4500 m deep (Bourillet et al., 2006; Mulder et al.,
107 2012; Fig. 1a). Four dendritic V-shaped branches are controlled by persistent headward
108 erosion, which creates sub-vertical walls with exposed Cretaceous to Pleistocene
109 sedimentary successions (Carter et al., 2018 and references therein). The sandwaves
110 presented in this study were previously interpreted as relict features active during the
111 Last Glacial Maxima (Cunningam et al., 2005). Two hundred km SE from the sandwave
112 field presented here, up to 1 km long active sandwaves were described on the La
113 Chapelle Bank, and interpreted as being controlled by barotropic (surface) tidal residual
114 velocities, although baroclinic (internal) tides could play a role in their dynamics in
115 proximity of the shelf-edge (Heathershaw and Codd, 1985).

116 Tidal currents in the Celtic Sea region are dominated by semi-diurnal (twice daily)
117 constituents and 75% of the kinetic energy can be attributed to the principal lunar semi-
118 diurnal constituent (M_2) (Pingree, 1980). Along the Celtic margin, barotropic tidal
119 currents vary in magnitude over the spring-neap cycle, from 0.2 m s^{-1} during neaps to
120 0.5 m s^{-1} during spring (Sharples et al., 2007). The semi-major axis of the M_2 tidal
121 ellipse is orientated NE-SW, across the slope (Pingree et al., 1999). This tidal ellipse
122 orientation, along with a density stratified water column, allows the generation of
123 internal waves with tidal frequencies (internal tides).

124 The highly corrugated slopes of the upper canyon and outer shelf generate a complex
125 internal tide field (Vlasenko et al., 2014) and on-shelf propagating waves are dissipated
126 close to the shelf-edge (Hopkins et al., 2014). Strong tidal currents and breaking internal
127 waves within Whittard Canyon are expected to enhance the turbulent mixing of physical
128 and biogeochemical properties through the water column, especially near the canyon
129 heads, and may also generate near-bed internal bores, which increase sediment

130 resuspension and along-canyon transport (Amaro et al., 2016; Hall et al., 2017; Aslam
131 et al., 2018).

132 **3. MATERIAL AND METHODS**

133 Most of the dataset used for this study has been collected during the JC125 Cruise,
134 carried out in 2015 aboard the RRS "James Cook", in the frame of the CODEMAP
135 Project ("Complex Deep-sea Environments: Mapping habitat heterogeneity As Proxy
136 for biodiversity" - ERC Starting Grant). The shipboard Multibeam (MB) system was the
137 100 kHz Kongsberg EM710, producing a Digital Terrain Model (DTM) at a grid cell
138 resolution of 5 m. An additional MB dataset, aimed to extend the mapping of bedforms
139 around the area, was collected with the same MB system in 2018 during the JC166
140 Cruise, aboard the RRS "James Cook" (part of the NERC funded CLASS programme).
141 Two AUV "Autosub6000" Side Scan Sonar (SSS) missions and one MB survey were
142 performed during JC125. AUV navigation was achieved using a RDI Doppler Velocity
143 Log (DVL) inertial navigation system (dead-reckoning) linked to a GPS fix before
144 descending and a Ultra-Short Baseline (USBL) position at the start of the mission. To
145 minimize the AUV drift during the dives, its position was also recalculated at the end of
146 each mission by USBL if the ship was in the vicinity, or by GPS surface location once
147 emerged.

148 The AUV-SSS was the 410 kHz EdgeTech FS2200. SSS mosaics were produced at a
149 grid cell resolution of 15 cm using the software PRISM, developed at the National
150 Oceanography Centre (NOC). The AUV-MB system was a 200 kHz Kongsberg
151 EM2040, allowing for the production of a DTM at a grid cell resolution of 2 m. The
152 ROV "ISIS" performed two dives on a western region where AUV-SSS was previously
153 acquired, to groundtruth the area using an integrated vibro-corer. The ROV-vibro-core
154 strongly improved the precision of sampling operations, in parallel with a visual

155 groundtruth of the local habitats. ROV navigation was achieved using a Sonardyne
156 USBL, in parallel with Doppler dead-reckoning calculated through a RDI DVL. Three
157 ROV vibro-cores were collected from different bedform settings (sand peak: VC_129,
158 sandwave stoss: VC_131-1, sandwave trough: VC_131-2) with penetrations of 98 cm,
159 74 cm and 43 cm respectively. The ROV camera was an OKEANOS Insite Mini Zeus
160 HD 1920 x 1080, equipped with two parallel laser pointers 10 cm apart. Two additional
161 box-cores were collected (sandwave stoss: BC_147, sandwave crest: BC_148) and sub-
162 sampled, resulting in core lengths of 19 cm and 20 cm respectively. Samples from
163 sediment cores were collected every 5 centimetres and dried at 80°C for 24 hours. The
164 sediment fraction finer than 2000 μm was examined using an LA-950V2 laser scattering
165 particle size distribution analyser (HORIBA), while the coarser fraction was sieved for
166 6000, 4000 and 2000 μm .

167 1270 bathymetric transects orthogonal to the sandwave crests and spaced 20 m each
168 other were extracted from the bathymetric grids, and morphometric indices (wavelength
169 λ , height h , asymmetry index (AI), migration rates) calculated. The sandwave
170 wavelength ($L=L_1+L_2$) is defined as the distance from trough to trough, compensated
171 for slope inclination α (Fig. 2). The sandwave height (h) is calculated as the orthogonal
172 from the highest point of the bedform (crest) to the baseline (Fig. 2). Following the
173 method of Knaapen (2005), the asymmetry index (AI) is defined as the difference of the
174 distances between the crest and the upslope and downslope troughs, divided by the
175 wavelength $(L_2-L_1)/L$ (Fig. 2). Positive and negative AI values are indicative of
176 downslope and upslope asymmetry respectively. Sandwaves with AI between -0.2 and
177 0.2 were considered as symmetric. Coordinates and elevations were obtained every 20
178 m along each transect. Hull-mounted MB bathymetry (15 m grid cell resolution)
179 acquired in 2000 by the Geological Survey of Ireland in the frame of the INFOMAR

180 Project was compared to the JC125 MB dataset (5 m grid cell resolution) to assess the
181 migration rate of the mapped sandwaves over a period of 15 years.

182

183 **4. RESULTS**

184 **4.1 Geomorphology of the Whittard bedforms**

185 The sandwave field was mapped across a 25 by 9 km wide sector of the outer shelf,
186 with a 0.1° gradient on average, within a depth range of 164-210 m (Fig.1b). The outer
187 shelf is incised between 200 m and 220 m by the heads of two adjacent tributaries of the
188 eastern branch of the Whittard Canyon, defined here as western and eastern tributaries
189 (Fig.1b). The average wavelength of the sandwaves is 367 m, with a maximum of 880
190 m (Fig. S1). Their height displays an average value of 4 m, with a maximum of 10.4 m
191 (Fig. S1). All sandwaves are approximately parallel to the shelf-edge, directed
192 perpendicular to the axes of the two tributaries (Fig. 1b).

193 Asymmetry is significantly different between the regions of mapped sandwaves (Fig. 3).
194 Sandwaves adjacent to the western tributary display up-slope asymmetric trends, with
195 average AI values of -0.3 and minimum of -0.95 (Fig. S1). At an average depth of 190
196 m, these sandwaves become symmetric for a limited portion of the shelf and become
197 down-slope asymmetric at shallower depths (Fig. 3). In the transition between up-slope
198 and down-slope asymmetry, all three trends can coexist on the same sandwaves,
199 reflecting convergent sediment transport directions (Fig. 3). Down-slope asymmetry
200 becomes dominant towards the easternmost sector of the shelf, where AI values display
201 an average of 0.29, increasing up to 0.9 (Fig. 3, Fig. S1). Two sub-areas (named western
202 and eastern fields hereafter) located 10 km apart in front of the western and eastern
203 tributaries, were mapped at high resolution with the AUV (Figs. 4-7, Fig. S2).

204 Furthermore, the western field was groundtruthed with ROV visual observations, vibro-
205 cores and box-cores.

206

207 *Western field* - The western field displays a sandwave train between 188 m and 240 m
208 water depth (Fig. 4). Their average wavelength is 387 m, with a maximum value of 671
209 m, the average height being 5.2 m, with a maximum value of 10.4 m (Fig. S3). The
210 western sandwaves are up-slope asymmetric (average value AI: -0.33, minimum value:
211 -0.94) (Fig. S3), with their asymmetry decreasing towards the shallower sectors,
212 suggesting a net sediment transport directed from the canyon head to the outer shelf
213 (Fig. 3). Crests, approximately parallel and occasionally bifurcated, are mostly NW-SE
214 oriented (120°) and up to 10 km long (Fig. 3). AUV-SSS mapping revealed that 2D
215 megaripples and complex 3D features occur on the entire western field (Figs. 4, 5).
216 Almost all the megaripples display an up-slope asymmetry, coherent with the
217 sandwaves on which they are superimposed (Fig. 8a).

218 At the head of the western tributary, at a depth between 205 m and 230 m, a dense
219 network of asymmetric megaripple trains occurs with a height of up to 1 m and a
220 variable wavelength ranging between 10 m and 45 m (Figs. 4, 5a). Along this sector,
221 megaripples organize in a herringbone pattern with a bimodal orientation: NW-SE
222 (140° - 160°) and WNW-ESE (100° - 110°) (Fig. 4). Moreover, megaripples here are
223 occasionally interrupted by longitudinally aligned sand peaks, alternating crests and
224 troughs for up to 110 m long in a NE-SW direction (47° - 60°) (Fig. 5a). Towards
225 shallower depths, megaripple wavelength decreases, ranging between 6 m and 14 m,
226 with the longest occurring close to the sandwave crests, and their height being 0.5 m on
227 average (Fig. 5b). Their main orientation is NW-SE (130° - 160°), forming a clockwise
228 angle of 10° - 40° offset with the sandwave crests (Figs. 4, 5). Megaripples are generally

229 absent on a low-energy "shadow zone" sheltered by the sandwave crests, in some case
230 displaying low backscatter facies suggesting fine sediment textures (Figs. 5b, c, d). The
231 shadow zone covers the troughs and which becomes progressively larger moving up-
232 slope (Fig. 4). In parallel, moving up-slope, megaripples concentrate exclusively on the
233 sandwave crests, losing their relief and lateral continuity (Figs. 4, 5c, 8a). The tallest
234 sandwaves of the western field display on their crests roughly circular depressions
235 regularly and closely spaced, 10-15 m wide, and up to 0.4 m deep (Fig. 5b). To our
236 knowledge, these intriguing features, defined as bowl-shaped depressions, have never
237 been described in previous works.

238

239 *Eastern field* - Sandwaves of the eastern field occur at a depth between 178 m and 201
240 m, where they are interrupted at the shelf margin, incised by the head of the eastern
241 tributary canyon (Fig. 1b, Fig. S2). They display an average wavelength of 324 m, with
242 a maximum value of 574 m, and an average height of 3.1 m, with a maximum value of
243 7.5 m (Fig. S3). The eastern sandwaves are NW-SE oriented (average orientation:
244 134°), their crests being linear or slightly sinuous. They present a positive asymmetry
245 index (average AI: 0.12, maximum AI: 0.78) (Fig. S3), being directed towards the head
246 of the tributary canyon and contrasting with the opposite trend of the western field (Fig.
247 S2). AUV-SSS and MB data collected on the eastern field display a dense network of
248 superimposed megaripple trains, 5 to 15 m long and up to 0.5 m high (Figs. 6,8b, Fig.
249 S2). These megaripples are observed on the sandwave stoss sides and close to the crests,
250 and are less frequent along the trough (Figs. 7a, 8b). They develop in a similar direction
251 to the sandwaves crests (NW-SE), or offset by a clockwise angle of $20-30^\circ$ with them
252 (Fig. 6). Their morphology ranges between slightly symmetrical to asymmetrical, with
253 their asymmetry increasing close to the sandwave crests and being consistent with the

254 sandwaves migrating towards the canyon (Fig. 8b). This is also reflected by the high
255 backscatter facies on some of the crests, suggesting coarse sediments controlled by
256 high-energetic hydrodynamics, changing to low backscatter on the following downslope
257 lee, coinciding with fine-sediment in sheltered low-energy environments (Figs. 7b,
258 7b1). The crests of the most pronounced sandwaves in the eastern field display in most
259 cases an uncommon two-fold morphology in plan view, consisting of two, or three,
260 megaripple crests running parallel to the sandwave crest (Figs. 6, 7b). The two-fold
261 crests can laterally pass to 3D geomorphologies, defined here as tear-drop shaped lobes,
262 0.4-0.8 m deep, stretching for 30 to 40 m along the direction of the sandwave crests
263 (Figs. 6, 7b).

264 Finally, a dense network of asymmetric megaripples directed towards deeper depths has
265 been mapped on the canyon head (Figs. 7c, d). These megaripples are 5 to 20 m long
266 and 0.5 to 0.8 m high. In limited areas of this region, megaripples merge their crests to
267 form 3D sub-circular features, 20-40 m wide and 0.5-1 m deep (Figs. 7c, d).

268 **4.2 Groundtruthing data**

269 *Sediment cores*

270 Vibro-cores (VC) and box-cores (BC) reveal a dominant sandy grain size, although their
271 spatial variability reflects different morpho-sedimentary environments within the
272 sampled bedforms. The core collected on a sand peak of the western field (VC_129,
273 Fig. 9a), consists of well sorted yellow medium sands throughout the entire 98 cm long
274 core, except for an increase to coarse and very coarse sands between 20 and 30 cm
275 below the surface (Fig. 9). The core does not present any stratification or internal
276 structure. Two cores were collected on the stoss side (VC_131-1) and in the trough
277 (VC_131-2) of the same sandwave (Fig. 9b). On the sandwave stoss side, where
278 superimposed megaripples are evident on the SSS mosaic (Fig. 9b), VC_131-1 consists

279 of greenish muddy layers for the first 3 cm, coarsening to well sorted brownish medium
280 sands until the depth of 38 cm (Fig 9). Below this level, sediment grain size changes to
281 moderately sorted medium sands with armouring gravelly layers consisting of scattered
282 broken shells, 1 to 2 cm large, down to the base of the core, at 74 cm (Fig. 9). In the
283 trough of the same sandwave, VC_131-2 shows bioturbated sediments with a finer
284 sediment texture, consisting of greenish poorly sorted muddy sands, becoming stiff
285 from 35 cm to the base of the core, 43 cm deep (Fig. 9). Coarse broken shells occur
286 between 12 and 15 cm and a layer of well laminated bioclasts (mainly Scaphopoda) is
287 evident between 28 and 31 cm, sustained by a matrix of medium and fine sands (Fig. 9).
288 Two box-cores were collected in the same region (Fig. 9). BC_147, located on the
289 sandwave crest, is dominated by well sorted and winnowed yellow medium sands,
290 without any internal structure across its length (21 cm). BC_148, 18 cm deep, is located
291 in the trough of the sandwave, nearby VC_131-2 (Fig. 9), and consists of strongly
292 bioturbated poorly sorted greenish silty fine sands. Several burrows inhabited by worms
293 were observed on the top and within the first 10 cm of this box-core (Fig. 9).

294

295 *Seabed video observations*

296 The ROV videos collected during the vibro-core operations show different aspects of
297 the seafloor in the sampled regions. The sampled sand peak is fully covered by
298 superimposed sharp-crested up-canyon asymmetric ripples and almost a total absence of
299 benthic fauna has been observed, except for a few sparse holothurians (Fig. 10a).
300 Relevant changes were observed in the ROV transect moving from VC_131-1 to
301 VC_131-2. The stoss region (location of VC_131-1) was characterized by faded up-
302 slope ripples and by the presence of mainly mobile fauna (starfish, crabs, holothurians,
303 fishes) (Fig. 10b). Getting close to the sandwave crest, fresh ripples were observed

304 superimposed on the megaripples, displaying the same orientation and asymmetric
305 trends (Figs. 10c, d). Similarly to the location of VC_129, very few organisms were
306 observed on the ROV video when approaching the crest (Figs. 10c, d). Down-slope of
307 the sandwave crest, ripples tended to fade out in the trough, coinciding with the region
308 of the SSS mosaic in which megaripples cease to occur. In parallel, bioturbation
309 increased, and several sessile organisms, mainly anemones, were observed at the
310 VC_131-2 sampling location (Fig. 10e).

311

312 **5. DISCUSSION**

313 **5.1 Up-slope and down-slope outer-shelf bedforms around the Whittard Canyon**

314 The application of advanced marine robotic technologies unveiled spectacular fields of
315 bedforms at the head of the Whittard Canyon. Up- and down-slope asymmetric
316 bedforms, spanning centimetre to kilometre scales, reflect the occurrence of peculiar
317 sediment dynamic processes which connect the outer shelf domain with the heads of
318 submarine canyons and vice versa. The bedforms are mainly composed of sandy
319 sediments, which most likely consist of coastal bioclastic deposits produced during
320 previous sea-level lowstands (Scourse et al., 2009) and reworked since the last sea-level
321 transgressive stage until the present day. The distribution, orientation and asymmetry
322 observed on the bedforms surrounding the head of the western tributary suggest that
323 these sandwaves are related to strong up-canyon near-bottom currents which rise up the
324 canyon rim onto the surrounding outer shelf (Fig. 11).

325 We rule out the interpretation of these bedforms as up-slope migrating cyclic steps, as
326 these features are generally controlled by channelized density currents on steep slopes,
327 alternating super and sub-critical flows (Parker, 1996; Paull et al., 2011; Slooman and
328 Cartigny, 2020). None of the above mentioned environmental conditions are observed

329 in the study area. The up-canyon migrating 3D megaripples and the aligned sand peaks
330 mapped at the head of this canyon (Figs. 4, 5a) probably reflect the most energetic
331 hydrodynamic regime of the entire study area, requiring up to 1 m s^{-1} fast currents to
332 form (Southard and Boguchwal, 1990). Both the directions of megaripples (NW-SE and
333 WNW-ESE) and of aligned sand peaks (NE-SW) are consistent with along-canyon-axis
334 near-bottom currents, orientated NE-SW.

335 Moreover, the ongoing action of strong up-slope flows is confirmed by the large
336 "shadow areas" on the stoss sides of the sandwaves, often coinciding with low
337 backscatter facies, and by the megaripples superimposed on the sandwaves (SSS
338 observation) (Figs. 5b, c, d), which in turn host fresh ripples (ROV visual observations)
339 (Figs. 10c, d), all of them displaying similar asymmetric trends and particularly
340 complex patterns around the sandwave crests (Figs. 4, 5b,d). The divergence angle of
341 20° - 35° between megaripple and sandwave crests is probably due to the deflection of
342 local flows induced by the variable geomorphology (Van Dijk and Kleinans, 2005).

343 Moving away from the canyon head, the intensity of up-slope bottom currents
344 progressively dissipates, with the megaripples fading on the sandwave stoss sides and
345 tending to develop exclusively on their crests (Fig. 4).

346 Up-slope bedform asymmetry ceases at around 190 m water depth, coinciding with the
347 upper limit of sandwave bifurcations, indicating that the canyon-sourced sediment
348 transport direction is limited to the region surrounding the canyon head (Figs. 3, 11).

349 Shallower and to the side of the canyon head, the sandwaves become symmetric and
350 transition to down-slope asymmetric (Figs. 3, 11). The orientation of down-slope
351 sandwaves coincides with the direction of the regional across-shelf tidal currents, which
352 have a dominant NE-SW direction (Amaro et al., 2016). On the deepest sector of the
353 shelf, at an average depth of 190 m, down-slope sandwaves are interrupted by the head

354 of the eastern tributary canyon, which incises the outer shelf deposits (Figs. 3, 6, 11).
355 The superimposed megaripples of the eastern field are equally down-slope asymmetric,
356 controlled by bottom currents directed towards the canyon head (Figs. 6, 7a, b), where
357 intense down-slope gravity currents can generate rounded 3D megaripples (Figs. 6c,d,
358 11). These bedform fields suggest that the Whittard Canyon is an active conduit for
359 sediment transport processes funnelling coarse sediments down to the deep sea.

360

361 **5.2 The role of Whittard Canyon in the generation and maintenance of up-slope** 362 **sandwaves**

363 To our knowledge, this work presents the first extensive seafloor expression of up-slope
364 bottom currents rising over the rim of a submarine canyon onto the outer shelf. Some
365 older works based on low-resolution geophysical datasets have described sandwave
366 dynamics hinting at similar hydrodynamic forcing along the upper reaches of other
367 canyons (Knebel and Folger, 1976; Karl et al., 1986). Seismic records revealed the
368 occurrence of up-slope asymmetric sandwaves at the head of Navariski Canyon (Bering
369 Sea) (Karl et al., 1986) and at the outer shelf adjacent to the head of Wilmington
370 Canyon (US Atlantic margin) (Knebel and Folger, 1976). The sandwaves, perpendicular
371 to the canyon axis, are composed of fine sands and resemble the dimensions of the
372 sandwaves described here. The suggested mechanisms responsible for sandwave
373 migration were in both cases internal waves with a tidal or shorter period, which once
374 channelized along the canyon axis would increase in strength and transport sediments
375 towards the canyon head (Knebel and Folger, 1976; Karl et al., 1986).

376 Barotropic tides over abrupt and sloping canyon morphologies can locally generate
377 internal tides (Hotchkiss and Wunsch, 1982; Hall and Carter 2011), and form up-slope
378 propagating internal tidal bores during critical or near-critical reflection (Dauxois and

379 Young, 1999; Legg and Adcroft, 2003). These conditions are met when the geometric
380 slope of internal tides (determined by wave frequency, stratification strength, and
381 latitude) is approximately equal to the canyon-axis morphological slope. During near-
382 critical reflection, internal wave energy is trapped near the sloping boundary and
383 typically results in non-linear effects, wave breaking, and, if the forcing internal tide is
384 strong enough, the formation of an internal bore (Hall et al., 2017). Oscillatory down-
385 and up-welling bottom flows with tidal or sub-tidal frequencies strongly increase their
386 intensity along the axis of several well-studied submarine canyons, most of them
387 located on the North Atlantic and North Pacific margins (Xu, 2011; Puig et al., 2013; Li
388 et al., 2019).

389 The Bay of Biscay shelf break, and canyons/corrugations along it, are energetic internal
390 tide generators (Vlasenko et al., 2014). Internal tides, generated at the shelf break by
391 across-slope tidal flows (Aslam et al., 2018 and references therein), have been observed
392 as a coherent signal in the internal wave field up to 170 km onto the Celtic Sea shelf
393 (Inall et al., 2011).

394 A high-resolution numerical simulation of the M_2 internal tide in the Whittard Canyon
395 (Aslam et al., 2018) suggests that the depth-integrated internal tide energy flux is highly
396 variable within the canyon and that the eastern branch, plus Explorer Canyon, Dangeard
397 Canyon and the flanks of Brenot Spur (Fig. 1) are key generation sites. The internal tide
398 is topographically steered along the canyon branches, but energy fluxes are directed
399 both up- and down-canyon, depending on the branch in question (Amaro et al., 2016;
400 Hall et al. 2017; Aslam et al., 2018). Close to the Whittard sandwave field, a
401 hydrographic mooring time-series accompanied by a fine-resolution 3D numerical
402 model simulation have revealed internal waves propagating north-east towards the
403 continental shelf each semi-diurnal tidal cycle together with internal solitary waves with

404 up to 105 m wide amplitudes (Vlasenko et al., 2014). In Whittard Canyon itself, near-
405 bed flows are dominated by moderate to strong semi-diurnal tidal currents orientated
406 along the canyon axis (van Weering et al., 2000; Amaro et al., 2016). Ocean glider and
407 hydrographic mooring time-series along the eastern tributary canyon have resolved
408 large-amplitude (up to 150 m in height) semi-diurnal internal tides (Hall et al., 2017; Dr
409 Furu Mienis, NIOZ, pers com; Fig. 11), possibly transitioning to asymmetrical-shaped
410 internal bores during spring tide (Hall et al., 2017). Therefore, we postulate that internal
411 tides are the responsible mechanism for up-slope sediment transport at the canyon head,
412 and up-slope sandwave orientation observed on the Whittard outer shelf. Our results
413 confirm the long-term persistence of overflowing bottom currents on the Whittard
414 Canyon heads (Fig. 11). The net sediment transport direction is the result of a complex
415 interplay between seafloor geomorphology and local hydrodynamics, consisting of
416 internal tides, surface tidal residual currents and gravitational currents. The semi-diurnal
417 internal tides interact with the rough geomorphology of the canyon head and of the
418 surrounding steep walls, and may generate strong up-slope propagating internal bores.
419 Geomorphological evidence indicates that the effect of up-slope internal waves is
420 almost entirely dissipated on the outer shelf at the depth of 195 m, at a distance of 5.5
421 km from the western tributary head (Fig. 3, 11). The reason for which up-slope
422 sandwaves are absent in the outer shelf adjacent to the eastern tributary is probably due
423 to the depth-constrained action of internal waves in this specific part of the canyon. The
424 eastern tributary cuts further into the shelf than the western tributary, giving place to the
425 abrupt morphology of the head up to a depth of 195 m (Fig. 11). The few symmetric and
426 up-slope sandwaves in front of the eastern tributary (Fig. 3) may represent the last
427 remnants of an old up-slope asymmetric field, which is now totally removed through the
428 retrogressive erosion of the canyon.

429

430 **5.3 Ongoing dynamics of the Whittard Canyon sandwaves**

431 There is a clear spatial variability of the contemporary sediment dynamics acting on the
432 Whittard Canyon sandwaves. The contrasting asymmetric patterns of the western and
433 eastern fields are consistent from cm to km scales, spanning ephemeral ripples to
434 megaripples and long-lived sandwaves (Fig. 8). This finding reveals a persistent
435 regional hydrodynamic regime, most probably controlled by the large-scale
436 geomorphology of the Whittard Canyon.

437 We assume that sandwaves were more active during previous lower sea level stages,
438 reflecting sediment dynamics and geomorphic patterns influenced by storm-induced and
439 tide-induced bottom currents, which during the last sea level rise progressively became
440 subordinate to the effect of the up- and down-slope flows, which currently dominate the
441 outer shelf. At the present time, the depth of the sandwaves prevents the significant
442 influence of storms, as observed in the nearby English Channel and North Sea deeper
443 than 80 m (e.g., Van Landeghen et al., 2012).

444 On a decadal perspective, comparative MB datasets collected 15 years apart (2000-
445 2015) do not suggest any measurable migration of sandwaves (Fig. S4). Carlson et al.
446 (1984) estimated an average migration rate of roughly 1 cm/yr for the sandwaves
447 observed on the head of the Navarinsky Canyon, which in our datasets would result in
448 sub-metric migrations below the spatial resolution of our hull-mounted MB dataset (Fig.
449 S4).

450 Although the Whittard Canyon sandwaves are apparently static on a metric scale, the
451 study area can be considered as a dynamic environment. The distribution of ripples and
452 megaripples, the observed changes in sediment composition and in the distribution of

453 benthic communities allowed some of the small-scale processes contributing to their
454 slow migration to be inferred.

455 - The sand peaks at the head of the western tributary are entirely constituted of
456 winnowed medium sands without any internal structure for the first 80 cm
457 (VC_129) (Fig. 9), suggesting the recent action of strong near-bottom flows.
458 Fresh up-slope asymmetric ripples superimposed on the peaks and the absence
459 of any fauna (Fig. 10a), unable to settle on sediments undergoing high physical
460 disturbance, is a further indication of recent strong hydrodynamics around the
461 canyon heads.

462 - On the sandwaves stoss sides, the 40 cm thick upper sandy sheet laying on
463 armoured bioclastic gravels and sands (VC_131-1, Fig. 9) currently represents
464 the most dynamic component of the sandwaves, moving over relict deposits
465 through the migration of megaripples, that have a similar height of 50-60 cm.
466 Migration of ripples and megaripples is known to influence the dynamics of the
467 larger sandwaves they superimpose (Naqshband et al., 2014).

468 - Sediment dynamics become more intense near the sandwave crests, which are
469 exclusively composed of winnowed coarse sands, with fresh asymmetric ripples
470 and bowl-shaped depressions over a seafloor deprived of any macrobenthic
471 fauna (BC_ 147 - Figs. 9b, 10c, d). This observation is coherent with the role of
472 crests in enhancing and steering bottom currents along them (Smyth, 2016). In
473 parallel, the crest area is characterized by the absence of any benthic fauna
474 which, similarly to what was observed on the sand peak, are probably unable to
475 settle on a habitat dominated by strong bottom current regimes (Figs. 10c, d).
476 The SSS mosaic at the eastern site (Fig. 6) also supports an interpretation of
477 higher current strengths around the sandwave crests, where megaripples are

478 focussed (Figs. 6, 7), generally increasing in density down-slope, towards the
479 canyon head (Figs. 7c, d).

480 On the other hand, several observations illustrate that the sediment dynamics is
481 discontinuous in space and time. The accumulation of a 3 cm thick muddy layer on
482 some sectors of the sandwave stoss sides (Fig. 9) reflects recent bedform inactivity in
483 this area. This is further evidenced by the occurrence of faded ripples and mobile
484 benthic fauna, which tolerate the action of medium to slow current regimes alternating
485 with isolated physical disturbance events (Harris, 2014) (Fig. 10b). In addition, at a
486 distance of 30 m ahead of the crest, the trough consists of bioturbated sandy sediments
487 within a reduced muddy matrix, reflecting a lower energy environmental setting
488 (BC_148, VC_131-2, Fig. 9). This is confirmed by faded ripples observed in the area
489 and by the occurrence of several sessile organisms (mainly anemones) colonizing the
490 seafloor (Fig. 10e). Preserved bioturbation structures and the homogeneous sedimentary
491 facies within the first 40 cm of the trough sub-surface (Fig. 9) further suggests a period
492 of stability and constant low-energy hydrodynamics persisting in this region over long-
493 term period, with an estimated temporal scale of at least several hundreds to a few
494 thousand years (Buffoni et al., 1992). The morpho-sedimentary characteristics shown by
495 the eastern SSS mosaic support a similar interpretation, with higher current strength
496 around the sandwave crests, where megaripples are focussed, and an increasing density
497 down-slope, towards the canyon head. Low backscatter facies along most of the lee
498 sides of both western and eastern fields most probably confirm that fine sediments
499 dominate these sectors, which are sheltered by the strong currents crossing the crests in
500 up- and downslope directions respectively (Figs. 4, 5b,c,d, 6, 7b). The strongest
501 hydrodynamics acting on the Whittard Canyon sandwaves are concentrated at the
502 canyon heads and the tallest crests and extend to the stoss sides only during the most

503 energetic events. Nonetheless, only the uppermost deposits of the sandwaves interact
504 with ongoing hydrodynamics and can promote bedform migration, whereas the deepest
505 and older sediment most likely consists of inactive and relict deposits, as already
506 described in other outer shelf settings (Goff and Duncan, 2012; Duran et al., 2018).
507 Finally, open-source EMODNET (European Marine Observation and Data Network)
508 bathymetric maps show that sandwave fields are largely present on most of the canyon
509 heads of the Celtic Margin. Although the low spatial resolution of these datasets does
510 not allow for clear quantification of sandwave asymmetry, semi-diurnal internal tides
511 are potentially an important process for enhancing up-slope sediment transport across
512 the shelf-edge of the entire Celtic margin, as already observed by Heathershaw and
513 Codd, 1985, and may be a dominant mechanism on regional scale.

514

515 **5.4 Bowl-shaped depressions: new findings on complex morpho-sedimentary** 516 **patterns along sandwave crests**

517 Fine scale AUV-SSS mosaics unveiled for the first time the bowl-shaped depressions.
518 These newly discovered morphologic features are present on most of the tallest crests of
519 the up-slope migrating sandwaves imaged in this study (Figs. 4, 5b). We hypothesize
520 that the sandwave crests on which two coexisting megaripples occur (Figs. 6, 7a, b)
521 most likely represent a precursor stage of the morpho-sedimentary process having the
522 bowl-shaped depressions as end-members (Fig. 12). The "two-fold" crest-trough-crest
523 morphology was observed on most of the eastern sandwaves (Fig. 6, 7b) and on sectors
524 of the western field, such as the crests of smaller secondary sandwaves and far from the
525 shelf-edge, which probably represent lower energy hydrodynamics (Figs. 4, 12a).
526 Megaripples around the sandwave crests can increase their sinuosity in response to local
527 hydrodynamic forcing, organize themselves in antithetic geometry, and create circular

528 to elongated tear-drop lobes stretched along the direction of crests (Figs. 7a, 12b, c).
529 When two antithetic megaripples merge, possibly under persisting and stronger
530 hydrodynamic conditions, they isolate residual portions of the troughs, generating
531 regular patterns of rounded bowl-shaped morphologies up to 0.6 m deep (Figs. 12d, e).
532 Assuming that megaripple trains migrate obliquely towards the sandwave crest, the
533 wavelength of megaripples and their orientation are responsible for the dimensions of
534 the bowl-shaped features, which resemble megaripples in both wavelength and height.
535 Despite these intriguing geomorphologies having never being observed in subaqueous
536 settings, similar spatial patterns have been described on the crests of terrestrial and
537 martian aeolian dunes controlled by bi-directional winds (Parteli et al., 2009; Courrech
538 du Pont et al., 2014). Meandering and antithetic dune crests occur under the alternate
539 action of oblique winds with divergence angles larger than 90° (Parteli et al., 2009;
540 Gadall et al., 2019). Under these conditions, bedforms align with the dominant direction
541 of the two flows, optimizing the maximum gross sediment transport able to maintain
542 them (Rubin and Hunter, 1987; Courrech du Pont et al., 2014; Gadall et al., 2019).
543 Bottom currents may increase their maximum bed shear stress approaching the crests of
544 the sandwaves, and steer secondary flows directed in the ebb direction (Gadall et al.,
545 2019), which could explain the along-crest elongation of some bowl-shaped depressions
546 (Fig. 11b). Moreover, field observations and 3D Computational Fluid Dynamics (CFD)
547 hint at an increased undulation of (sandwave) crest line and the action of oblique winds
548 as dominant parameters in producing deflected reverse flows, forming stretched
549 corkscrew vortices parallel to the dune (Delgado-Fernandez 2013; Jackson et al., 2013;
550 Smyth, 2016).
551 The bowl-shaped depressions around the head of the Whittard Canyon only develop on
552 the crests of the tallest sandwaves (Fig. 4), suggesting the crucial role of sandwave

553 height which, as observed on sub-aerial settings, can alter local hydrodynamics
554 producing higher energetic regimes around the crests (Smyth, 2016; Gadal et al., 2019).
555 Where bowl-shaped depressions occur, morphologic evidence resembles some of the
556 above mentioned pre-conditioning factors, with megaripples producing a rough
557 undulation of the sandwave crest line and their orientation (the assumed direction of
558 primary flows - red arrow in Fig. 12d) forming angles from 60° to 120° with the
559 sandwave crests (the assumed direction of secondary flows - blue arrow in Fig. 12d).
560 Nonetheless, without the acquisition of repeated mapping and long hydrodynamic time-
561 series, and an awareness that subaqueous and subaerial mechanisms may yield
562 substantial differences, a definitive understanding of the dynamics related to these
563 features still remains unclear and speculative.

564

565 **6. CONCLUSIONS**

566 The application of multiple resolution geophysical mapping, including cutting-edge
567 marine robotics, unveiled uncommon up- and down-slope active bedform fields at the
568 head of the Whittard Canyon, displaying variability in intensity and direction of
569 sediment transport within a few hundreds of meters. The bedforms recognized in the
570 study area are sandwaves, megaripples, ripples, original sand peaks, and newly
571 discovered features along the sandwave crests, such as two-fold crests, tear-drop lobes
572 and bowl-shaped depressions.

573

574 Hydrodynamics inferred from asymmetric patterns of bedforms is consistent from cm
575 (ripples) to m (megaripples) and km (sandwaves) scales, suggesting a persistent regime
576 in the area maintained by the large-scale geomorphology of the Whittard Canyon head.

577

578 Large-amplitude semi-diurnal internal tides transitioning to asymmetric internal bores
579 under near-critical reflection, are the suspected mechanisms for the generation of strong
580 up-canyon bottom currents, deduced to be up to 1 m/s, overflowing the canyon rim to
581 the outer shelf and generating up-slope bedform fields in the outer shelf deeper than 190
582 m. Shallower, up-slope currents generated in the canyon lose intensity, and downslope
583 bedforms fields are preferentially developed.

584

585 Based on fine-scale observations, the strongest hydrodynamics, able to produce sediment
586 transport, are concentrated at the heads of the two studied tributary canyons and at the
587 tallest sandwave crests, where spectacular trains of bowl-shaped depressions, never
588 observed before, suggest self-organizing patterns of megaripples, in response to bi-
589 directional current regimes interacting with a complex geomorphology.

590

591 Nonetheless, only the uppermost sediments of the sandwaves promote ongoing bedform
592 activity through ripples and megaripples migration, whereas the deepest sediments seem
593 to remain inactive as relict deposits.

594

595 Our results demonstrate the paramount importance of high-resolution methodologies in
596 the study of deep water settings like active bedform fields, yielding relevant insights on
597 the dynamics of complex environments, with implications in geo-hazard assessment for
598 industrial infrastructures and exchange of carbon-rich particles across shelf/slope fronts.

599

600 **7. ACKNOWLEDGEMENTS**

601 Most of the data used in this work has been acquired in the JC125 cruise, funded by the

602 ERC CODEMAP project (Complex Deep-sea Environments: Mapping habitat
603 heterogeneity As Proxy for biodiversity) (Grant No. 258482, PI: Dr V.A.I. Huvenne).
604 Additional data have been collected in the frame of the NERC funded CLASS
605 programme, Grant No. NE/R015953/1. We acknowledge the captain and crew of the
606 RRS James Cook for their assistance during the JC125 and JC166 expeditions. Special
607 thanks go to Tim Le Bas for processing the AUV-SSS and AUV-MB maps, and to the
608 ROV "ISIS" team for their kind cooperation during data acquisition. The 2000 MB
609 dataset has been collected in the frame of the INFOMAR project (Integrated Mapping
610 for the Sustainable Development of Ireland's Marine Resources). We are finally
611 indebted with Dr P. Puig, for the fruitful discussions we had during the production of
612 this work, and with Dr. F. Mienis for her kindness in sharing information on
613 hydrographic mooring time-series. Gareth Carter publishes with permission of the
614 Director of the British Geological Survey (United Kingdom Research and Innovation).

615

616 **8. REFERENCES**

617 Ahmerkamp, S., Winter, C., Janssen, F., Kuypers, M.M.M., Holtappels, M., 2015. The
618 impact of bedform migration on benthic oxygen fluxes. *J. Geophys. Res.* 120, 2229–
619 2242. doi:10.1002/2015JG003106.

620

621 Amaro, T., Huvenne, V.A.I., Allcock, A.L., Aslam, T., Davies, J.S., Danovaro, R., De
622 Stigter, H.C., Duineveld, G.C.A., Gambi, C., Gooday, A.J., Gunton, L.M., Hall, R.,
623 Howell, K.L., Ingels, J., Kiriakoulakis, K., Kershaw, C.E., Lavaleye, M.S.S., Robert,
624 K., Stewart, H., Van Rooij, D., White, M., Wilson, A.M., 2016. The Whittard Canyon –
625 a case study of submarine canyon processes. *Prog. Oceanogr.* 146, 38–57.

626

627 Allen, S.E., Durrieu de Madron, X., 2009. A review of the role of submarine canyons in
628 deep-ocean exchange with the shelf *Ocean Sci.*, 5, 607–620,. [www.ocean-](http://www.ocean-sci.net/5/607/2009/)
629 [sci.net/5/607/2009/](http://www.ocean-sci.net/5/607/2009/)
630

631 Aslam, T., Hall, R. A., Dye, S. R., 2018. Internal tides in a dendritic submarine canyon.
632 *Progress in Oceanography* 169, 20-32. doi:10.1016/j.pocean.2017.10.005.
633

634 Azpiroz-Zabala, M., Cartigny, M.J.B., Talling, P.J., Parsons, D.R., Sumner, E.J., Clare,
635 M.A., Simmons, S.M., Cooper, C., Pope, E., 2017. Newly recognized turbidity current
636 structure can explain prolonged flushing of submarine canyons. *Science advances* 3-10,
637 doi: 10.1125/sciadv1700200
638

639 Berné, S., Laricolais, G., Marsset, T., Bourillet, J.F., De Batist, M., 1998. Erosional
640 offshore sand ridges and lowstand shorefaces: examples from tide- and wave-dominated
641 environments of France. *Journal of Sedimentary Research* 68, 540-555.
642

643 Bouysse, P., Horn, R. Lapierre, F., Le Lann, F., 1976. Etude des grands bancs de sable
644 du sud-est de la Mer Celtique, *Marine Geology* 20, 251-275.
645

646 Bourillet, J.F., Zaragosi, S., Mulder, T., 2006. The French Atlantic margin and deep-sea
647 submarine systems. *Geo-Marine Letters* 26, 311–315.
648

649 Buffoni, G., Delfanti, R., Papucci, C., 1992. Accumulation rates and mixing processes
650 in near-surface North Atlantic sediments: Evidence from C-14 and Pu-239,240
651 downcore profiles. *Marine Geology* 109 (1-2), 159-170.

652

653 Carlson, P.R, Fischer J.M., Karl, H.A., Larrdn, C., 1984. Isopach map of Seismic Unit
654 A, youngest sedimentary sequence in Navarin basin, in Karl, H. A., and Carlson, P. R.,
655 eds., Surface and Near-Surface Geology, Navafin Basin Province: results of the 1980-
656 81 field seasons: U.S. Geol. Survey Open-File Report 84-89, p. 33-38.

657

658 Carter, G.D.O., Huvenne, V.A.I., Gales, J.A., Lo Iacono, C., Marsh, L., Ougier-
659 Simonine A., Robert, K., Wynn, R.B., 2018. Ongoing evolution of submarine canyon
660 rockwalls; examples from the Whittard Canyon, Celtic Margin (NE Atlantic). Progress
661 in Oceanography 169, 79-88. doi: 10.1016/j.pocean.2018.02.001.

662

663 Courrech du Pont, S., Narteau, C., Gao, X., 2014. Two modes for dune orientation.
664 Geology 42-9, 743–746.

665

666 Cunningham, M.J., Hodgson, S., Masson, D.G., Parson, L.M., 2005. An evaluation of
667 along-and down-slope sediment transport processes between Goban Spur and Brenot
668 Spur on the Celtic Margin of the Bay of Biscay. Sedimentary Geology 79-1, 99–116.

669

670 Dauxois, T., Young W.R., 1999. Near Critical Reflection of Internal Waves. Journal of
671 Fluid Mechanics 390. doi: 10.1017/S0022112099005108.

672

673 Delgado-Fernandez, I., Jackson, D.W.T., Cooper, J.A.G., Baas, A.C.W., Beyers, J.H.,
674 Lynch, K., 2013. Field characterization of three-dimensional lee-side airflow patterns
675 under offshore winds at a beach-dune system. Journal of Geophysical Research - Earth
676 Surface 118, 706–721.

677

678 Durán, R., Guillén, J., Rivera, J., Lobo, F.J., Muñoz, A., Fernández-Salas, L.M., Acosta,
679 J., 2018. Formation, evolution and present-day activity of offshore sand ridges on a
680 narrow, tideless continental shelf with limited sediment supply. *Marine Geology* 397,
681 93–107.

682

683 Gadall, C., Narteau, C., Courrech du Pont, S., Rozier, O., Claudin, P., 2019. Incipient
684 bedforms in a bidirectional wind regime. *Journal of Fluid Mechanics* 862, 490-516. doi:
685 <https://doi.org/10.1017/jfm.2018.978>

686

687 Goff, J.A., Duncan, L.S., 2012. Re-examination of sand ridges on the middle and outer
688 New Jersey shelf based on combined analysis of multibeam bathymetry and backscatter,
689 seafloor grab samples and chirp seismic data. *Int. Assoc. Sedimentol. Spec. Publ.* 44,
690 121–142.

691

692 Hall, R.A., Carter, G.S., 2011. Internal tides in Monterey Submarine Canyon. *Journal of*
693 *Physical Oceanography* 41, 186–204. <http://dx.doi.org/10.1175/2010JPO4471.1>.

694

695 Hall, R.A., Aslam, T., Huvenne, V.A.I., 2017. Partly standing internal tides in a
696 dendritic submarine canyon observed by an ocean glider. *Deep Sea Research Part I* 126,
697 73–84, doi:10.1016/j.dsr.2017.05.015.

698

699 Harris, P.T., 2014. Shelf and deep-sea sedimentary environments and physical benthic
700 disturbance regimes: a review and synthesis. *Marine Geology* 353, 169–184.

701

702 Heathershaw, A.D., Codd, J.M., 1985. Sandwaves, internal waves and sediment
703 mobility at the shelf-edge in the Celtic Sea. *Oceanologica Acta* 8-4, 391-404.
704

705 Hotchkiss, F.S., Wunsch, C., 1982. Internal waves in Hudson Canyon with possible
706 geological implications. *Deep-Sea Research Part I* 29, 415-442.
707

708 Hopkins, J.E., Stephenson, G.R., Green, J., Inall, M.E., Palmer, M.R., 2014. Storms
709 modify baroclinic energy fluxes in a seasonally stratified shelf sea: inertial-tidal
710 interaction. *Journal of Geophysical Research - Oceans* 119, 6863–6883.
711

712 Inall, M., Aleynik, D., Boyd, T., Palmer, M., Sharples, J., 2011. Internal tide coherence
713 and decay over a wide shelf sea. *Geophysical Research Letters* 38, L23607,
714 doi:10.1029/2011GL049943.
715

716 Jackson, D.W.T., Beyers, M., Delgado-Fernandez, Irene., Baas, Andreas C.W., Cooper,
717 A. J., Lynch, Kevin., 2013. Airflow reversal and alternating corkscrew vortices in
718 foredune wake zones during perpendicular and oblique offshore winds. *Geomorphology*
719 187, 86–93. <http://dx.doi.org/10.1016/j.geomorph.2012.12.037>.
720

721 Jiang, W., Lin, M., 2016. Research on bilateral reverse migration of one-group seabed
722 sand waves in a small shallow shelf sea. *Coastal Engineering* 111, 70–82.
723

724 Karl, H.A., Cacchione D.A., Carlson P.R., 1986. Internal-wave currents as a mechanism
725 to account for large sand wave in Navarinsky Canyon head, Bering Sea. *Journal of*
726 *Sedimentary Petrology* 56-5, 706-714.

727

728 Knaapen, M.A.F., 2005. Sandwave migration predictor based on shape information.
729 *Journal of Geophysical Research* 110, F04S11, doi:10.1029/2004JF000195

730

731 Knebel, H.J., Folger, D.W., 1976. Large sand waves on the Atlantic outer-continental
732 shelf around Wilmington Canyon, off eastern United States: *Marine Geology* 22, 7-15.

733

734 Legg, S., Adcroft, A., 2003. Internal Wave Breaking at Concave and Convex
735 Continental Slopes. *Journal of Physical Oceanography* 33, 2224-2246.
736 [https://doi.org/10.1175/1520-0485\(2003\)033<2224:IWBACA>2.0.CO;2](https://doi.org/10.1175/1520-0485(2003)033<2224:IWBACA>2.0.CO;2)

737

738 Li, M.Z., Prescott, R.H., Robertson, A.G., 2019. Observation of internal tides and
739 sediment transport processes at the head of Logan Canyon on central Scotian Slope,
740 eastern Canada. *Journal of Marine Systems* 193, 103–125.
741 <https://doi.org/10.1016/j.jmarsys.2019.02.007>.

742

743 Lo Iacono, C., Guillén, J., Puig, P., Ribó, M., Ballesteros, M., Palanques, A., Farrán,
744 M., Acosta, J., 2010. Large-scale bedforms along a tideless outer shelf setting in the
745 Western Mediterranean. *Continental Shelf Research* 30, 1802-1813.

746

747 Mulder, T., Zaragosi, S., Garlan, T., Mavel, J., Cremer, M., Sottolichio, A., Sénéchal,
748 N., Schmidt, S., 2012. Present deep-submarine canyons activity in the Bay of Biscay
749 (NE Atlantic). *Marine Geology* 295–298, 113–127.

750

751 Naqshband, S., Ribberink, J.S., Hurther, D., Hulscher, S.M.J.H., 2014. Bed load and
752 suspended load contributions to migrating sand dunes in equilibrium. *Journal of*
753 *Geophysical Research - Earth Surface* 119, 1043–1063, doi:10.1002/2013JF003043.
754

755 Pantin, H.M., Evans, C.D.R., 1984. The Quaternary history of the central and
756 southwestern Celtic Sea. *Marine Geology* 57, 259--293.
757

758 Parker, G., 1996. Some speculations on the relation between channel morphology and
759 channel-scale flow structures, in Ashworth, P.J., et al., eds., *Coherent flow structures in*
760 *open channels*: Chichester, Wiley, p. 423–459.
761

762 Parteli, E.J.R., Durán, O., Tsoar, H., Schwämmled, V., Herrmann, H.J., 2009. Dune
763 formation under bimodal winds. *PNAS* December 29, 2009 vol. 106 no. 52 22085-
764 22089.
765

766 Paull, C., Caress, D.W., Ussler, W., Lundsten, E., Meiner-Johnson, M., 2011. High-
767 resolution bathymetry of the axial channels within Monterey and Soquel submarine
768 canyons, offshore central California. *Geosphere* 7-5, 1077–1101. doi:
769 10.1130/GES00636.1.
770

771 Pingree, R., 1980. *Physical oceanography of the Celtic sea and English channel*.
772 *Elsevier Oceanography Series* 24, 415–465.
773

774 Pingree, R.D., Sinha, B., Griffiths, C.R., 1999. Seasonality of the European slope
775 current (Goban Spur) and ocean margin exchange. *Continental Shelf Research* 19, 929–
776 975.
777

778 Piper, D.J.W., Normark, W.R., 2009. Processes that initiate turbidity currents and their
779 influence on turbidites: a marine geology perspective. *Journal of Sedimentary Research*
780 79, 347–362.
781

782 Praeg, D., McCarron, S., Dove, D., Ó Cofaigh, C., Scott, G., Monteys, X., Facchin, L.,
783 Romeo, R., Coxon, P., 2015. Ice sheet extension to the Celtic Sea shelf edge at the Last
784 Glacial Maximum. *Quaternary Science Reviews* 111, 107–112.
785

786 Puig, P., Greenan, B.J.W., Li, M.Z., Prescott, R.H., Piper, D.J.W., 2013. Sediment
787 transport processes at the head of Halibut Canyon, eastern Canada margin: an interplay
788 between internal tides and dense shelf-water cascading. *Marine Geology* 341, 14–28.
789

790 Reynaud, J.Y., Tessier, B., Berné, S., Chamley, H., de Batist, M., 1999. Tide and wave
791 dynamics on a sand bank from the deep shelf of the Western Channel approaches. *Marine
792 Geology* 161, 339–359.
793

794 Rovere, M., Pellegrini, C., Chiggiato, J., Campiani, E., Trincardi, F., 2019. Impact of
795 dense bottom water on a continental shelf: an example from the SW Adriatic Sea. *Marine
796 Geology* 408, 123–142. doi:10.1016/j.margeo.2018.12.002.
797

798 Rubin, D.M., Hunter, R.E., 1987. Bedform Alignment in Directionally Varying Flows.
799 Science 237, 276-278.
800

801 Scourse, J., Uehara, K., Wainwright, A., 2009. Celtic Sea linear tidal sand ridges, the
802 Irish Sea Ice Stream and the Fleuve Manche: palaeotidal modelling of a transitional
803 passive margin depositional system. Marine Geology 259, 102e111.
804

805 Sharples, J., Tweddle, J.F., Mattias Green, J., Palmer, M.R., Kim, Y.N., Hickman, A.E.,
806 Holligan, P.M., Moore, C.M., Rippeth, T.P., Simpson, J.H., et al., 2007. Spring-neap
807 modulation of internal tide mixing and vertical nitrate fluxes at a shelf edge in summer.
808 Limnology and Oceanography 52, 1735–1747.
809

810 Slooman, A., Cartigny, M.J.B., 2020. Cyclic steps: review and aggradation based
811 classification. Earth-Science Reviews 201, 102949.
812 <https://doi.org/10.1016/j.earscirev.2019.102949>
813

814 Smyth, T.A.G., 2016. A review of Computational Fluid Dynamics (CFD) airflow
815 modelling over aeolian landforms. Aeolian Research 22, 153–164.
816

817 Southard, J.B., Boguchwal, L.A., 1990. Bed configuration in steady unidirection water
818 flows. Part 2. Synthesis. Journal of Sedimentary Petrology 60-5. 658-679.
819

820 Van Landeghem, K.J.J., Baas, J.H., Mitchell, N.C., Wilcockson, D., Wheeler, A.J.,
821 2012. Reversed sediment wave migration in the Irish Sea, NW Europe: A reappraisal of

822 the validity of geometry-based predictive modelling and assumptions. *Marine Geology*
823 295–298, 95–112.

824

825 van Weering, T.C.E., Thomsen, L., van Heerwaarden, J., Koster, B., Viergutz, T., 2000.

826 A seabed lander and new techniques for long term in situ study of deep-sea near bed
827 dynamics. *Sea Technology* 41, 17–27.

828

829 Vlasenko, V., Stashchuk, N., Inall, M.E., Hopkins, J.E., 2014. Tidal energy conversion
830 in a global hot spot: on the 3-d dynamics of baroclinic tides at the Celtic sea shelf break.

831 *Journal of Geophysical Research - Oceans* 119, 3249–3265.

832

833 Xu, J.P., 2011. Measuring currents in submarine canyons: technological and scientific
834 progress in the past 30 years. *Geosphere* 7, 868–876.

835

836 **9. FIGURE CAPTIONS**

837 **Figure 1:** a) Multibeam bathymetric map of the Whittard Canyon, composed of MB
838 data belonging to NOC, INFOMAR Project (Integrated Mapping For The Sustainable
839 Development Of Ireland's Marine. Resource Programme.- Marine Institute and
840 Geologic Survey of Ireland) and EU Emodnet Project (European Marine Observation
841 and Data Network - Bathymetry Data Portal). EC: Explorer Canyon. DC: Dangeard
842 Canyon; b) bedform fields presented in this study, mapped at the heads of two tributary
843 canyons of the Whittard eastern branch (western and eastern tributaries). Ellipsoid
844 projection: WGS84.

845

846 **Figure 2:** Schematic representation and nomenclature of the sandwave characteristics
847 used in this study: L , wavelength; $L1$ and $L2$, lee and stoss side wavelength,
848 respectively; h , dune height (with slope correction); Z_c , crest depth; $Z1$ and $Z2$, trough
849 depth; X_c , $X1$ and $X2$, position of the sandwave crest and troughs along the bathymetric
850 profile; α , slope angle.

851

852 **Figure 3:** Asymmetry indexes of the Whittard Canyon sandwaves, classified in upslope
853 asymmetric (red, $AI < -0.25$), symmetric (white, $-0.25 < AI < 0.25$), and downslope
854 asymmetric (blue, $AI > 0.25$). Black dashed lines indicate the tracks of bathymetric
855 profiles illustrated in panels 1 and 2. Arrows in bathymetric profiles reflect the direction
856 of sediment transport deduced by sandwave asymmetry and the colour of asymmetry
857 classes. Ellipsoid projection: WGS84.

858

859 **Figure 4:** 15 cm grid cell resolution AUV-SSS mosaic acquired on the western field
860 sandwaves. Lighter shades correspond to higher backscatter. The white dashed line
861 coincides with the track of the below bathymetric profile. Numbers indicate the major
862 sandwaves of this sector.

863

864 **Figure 5:** Enlargements of the western AUV-SSS mosaic (Figure 4) and corresponding
865 bathymetric profiles (yellow dashed lines). Lighter shades correspond to higher
866 backscatter. Orange dashed lines in 5a indicate the longitudinal axes of numbered sand
867 peaks. bsd in c and $c1$: bowl-shaped depression. BS in b and d: backscatter. Low BS
868 acoustic facies are observed in figures b, c and d on the lee side and part of the trough,
869 likely indicating fine sediment areas, sheltered by strong upslope bottom currents.
870 Locations shown in Figure 4.

871

872 **Figure 6:** 15 cm grid cell resolution AUV-SSS mosaic acquired on the eastern field
873 sandwaves. Lighter shades correspond to higher backscatter. The white dashed line
874 coincides with the track of the below bathymetric profile. Numbers indicate the major
875 sandwaves of this sector.

876

877 **Figure 7:** Enlargements of the eastern AUV-SSS mosaic (Figure 6) and corresponding
878 bathymetric profiles (yellow dashed lines). Locations shown in Figure 6. High and low
879 backscatter (BS) acoustic facies are observed on the stoss and lee side of figure 7b,
880 likely indicating coarse vs fine sediment areas, respectively exposed to and sheltered by
881 downslope bottom currents.

882

883 **Figure 8:** Vectors of sediment transport direction deduced from sandwave (white
884 arrows) and megaripple (orange arrows) asymmetry. Criteria for defining asymmetric
885 trends are the same adopted in Figure 3. Density of megaripples (exclusively occurring
886 where orange arrows are depicted) increase downslope, towards the heads of both
887 western and eastern tributaries. Symmetric megaripples are more numerous in the
888 eastern field, likely evolving under the bidirectional action of tidal currents at the
889 bottom.

890

891 **Figure 9:** Enlargements of the AUV-SSS mosaic of western field (locations in Figure 4)
892 showing in a): the sand peak where the ROV-vibro-core VC_129 (red dot) was
893 retrieved; in b): the sandwave where the ROV-vibro-cores VC_131-1, VC_131-2
894 (orange and green dots, respectively) and the box-cores BC_147, BC_148 (dark and
895 light blue, respectively) were retrieved. BS stands for backscatter. Lighter shades
896 correspond to higher backscatter. Red crosses correspond to the location of ROV

897 images showed in Figure 10. Yellow dashed lines correspond to the tracks of the below
898 bathymetric profiles. Numbers in (a) correspond to the crests along the peaks. The
899 bathymetric profile of (b) coincides with the track of the ROV dive during which the
900 vibro-cores were collected. Arrows on bathymetric profiles coincide with the location of
901 retrieved samples. Below graphs show granulometric composition and photos of the
902 cores.

903

904 **Figure 10:** Bathymetric profiles (same tracks of Figure 9) and video-images from ROV
905 dives on the sampled sand peak (a; Figure 9a), and on the stoss (b) crest (c, d) and
906 trough (e) of the sampled sandwave (Figure 9b). Figures 10 a, b and e correspond to the
907 exact locations where VB129, 131-1 and 131-2 have been collected respectively.

908

909 **Figure 11:** 3D bathymetric sketch illustrating the main hydrodynamic and sedimentary
910 processes occurring in the study area. Up-slope bottom currents dominate the outer shelf
911 adjacent to the western tributary for a depth range of 190-220 m, whereas the eastern
912 tributary, carving the outer shelf for this depth range, is dominated by downslope
913 currents, being channelized within the gullies of the canyon head. Dots on the eastern
914 canyon axis correspond to the locations where an ocean glider (red dot, Hall et al.,
915 2017) and a hydrographic mooring (yellow dot, Dr Furu Mienis, pers. comm.) resolved
916 large-amplitude semi-diurnal internal tides.

917

918 **Figure 12:** Proposed evolutionary model of bowl-shaped depressions, originating from
919 megaripples crests laying on sandwave crests (two-fold crests, a) under the action of bi-
920 directional current regimes, transitioning to tear-drop lobes (b, c) and to bowl-shaped
921 depressions (d), regularly spaced along the sandwave crests (e). Red arrow indicates the

922 direction of dominating bottom currents, deduced from megaripple orientation; blue
923 arrow indicates the orientation of secondary currents, generated from the interaction of
924 current flows with the articulated morphology of sandwave crests. Lighter shades
925 correspond to higher backscatter.

926

927 **Figure S1:** Morphometric characteristics (wavelength, height and asymmetry) of the
928 Whittard Canyon sandwaves.

929

930 **Figure S2:** 25 cm grid cell resolution AUV-MB map of the eastern sandwave field.

931

932 **Figure S3:** Morphometric characteristics (wavelength, height and asymmetry) of the
933 sandwaves of western and eastern field.

934

935 **Figure S4:** Sandwave migration rates obtained by comparing two bathymetric grids
936 acquired 15 years apart. Note that the comparative 2000 MB grid used to estimate
937 potential migration has a pixel resolution of 15 m. Migrations within a distance of
938 around 20 m, corresponding to up around 90% of measurements, are therefore
939 considered as bias, and not taken into consideration. Estimates of rates larger than 20 m
940 are considered as artefacts.

Figure1_Lo lacono et al., 2019
[Click here to download high resolution image](#)

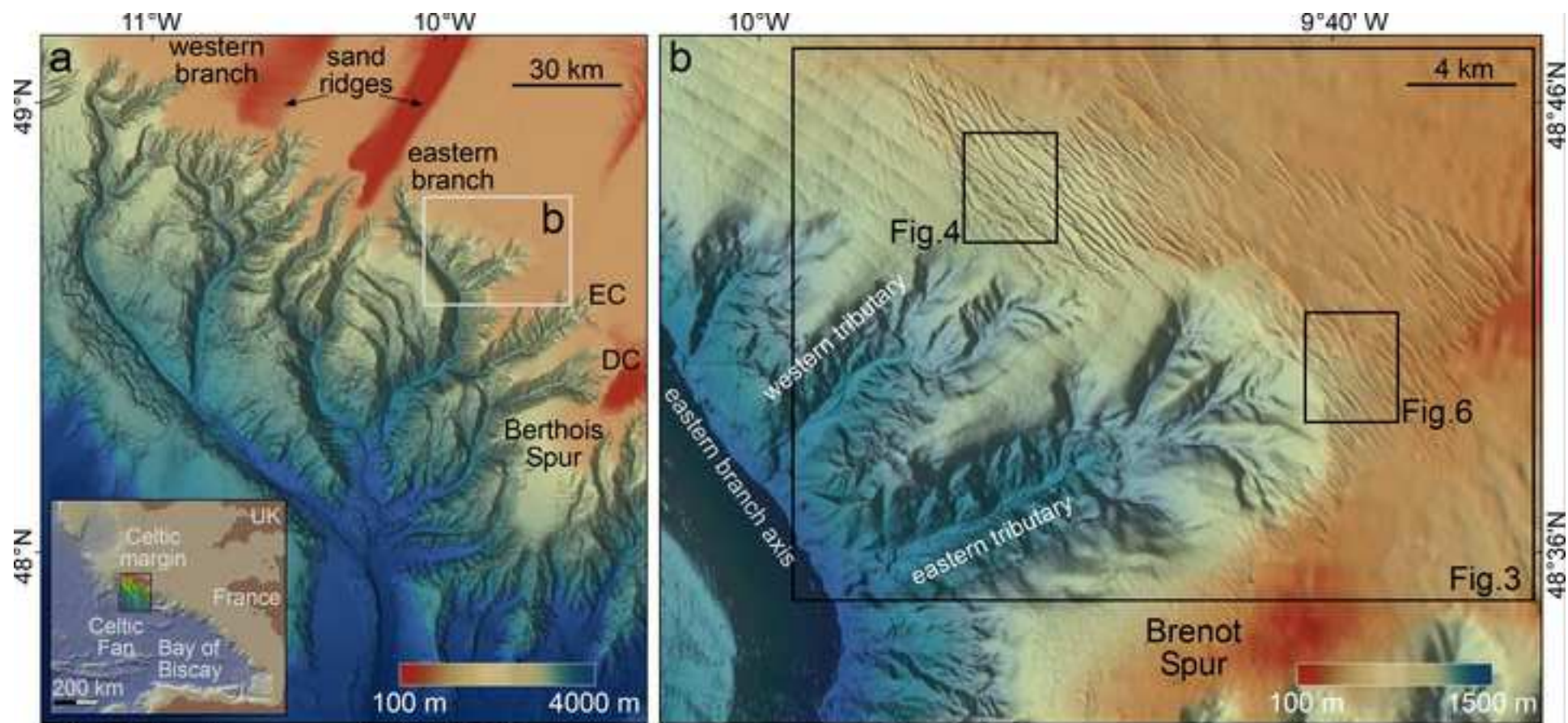


Fig.1 - Lo lacono et al., 2019

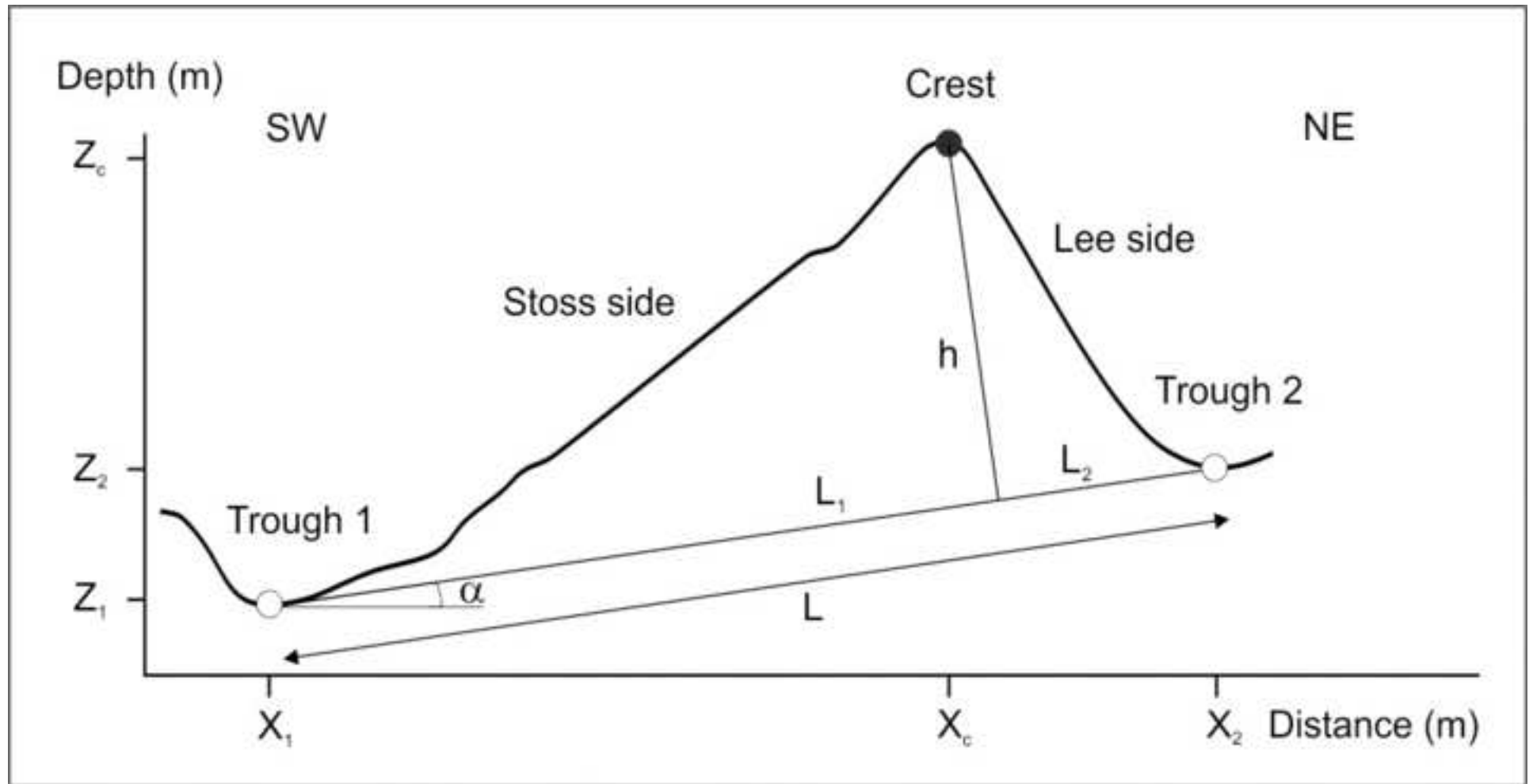


Figure3_Lo lacono et al., 2019
[Click here to download high resolution image](#)

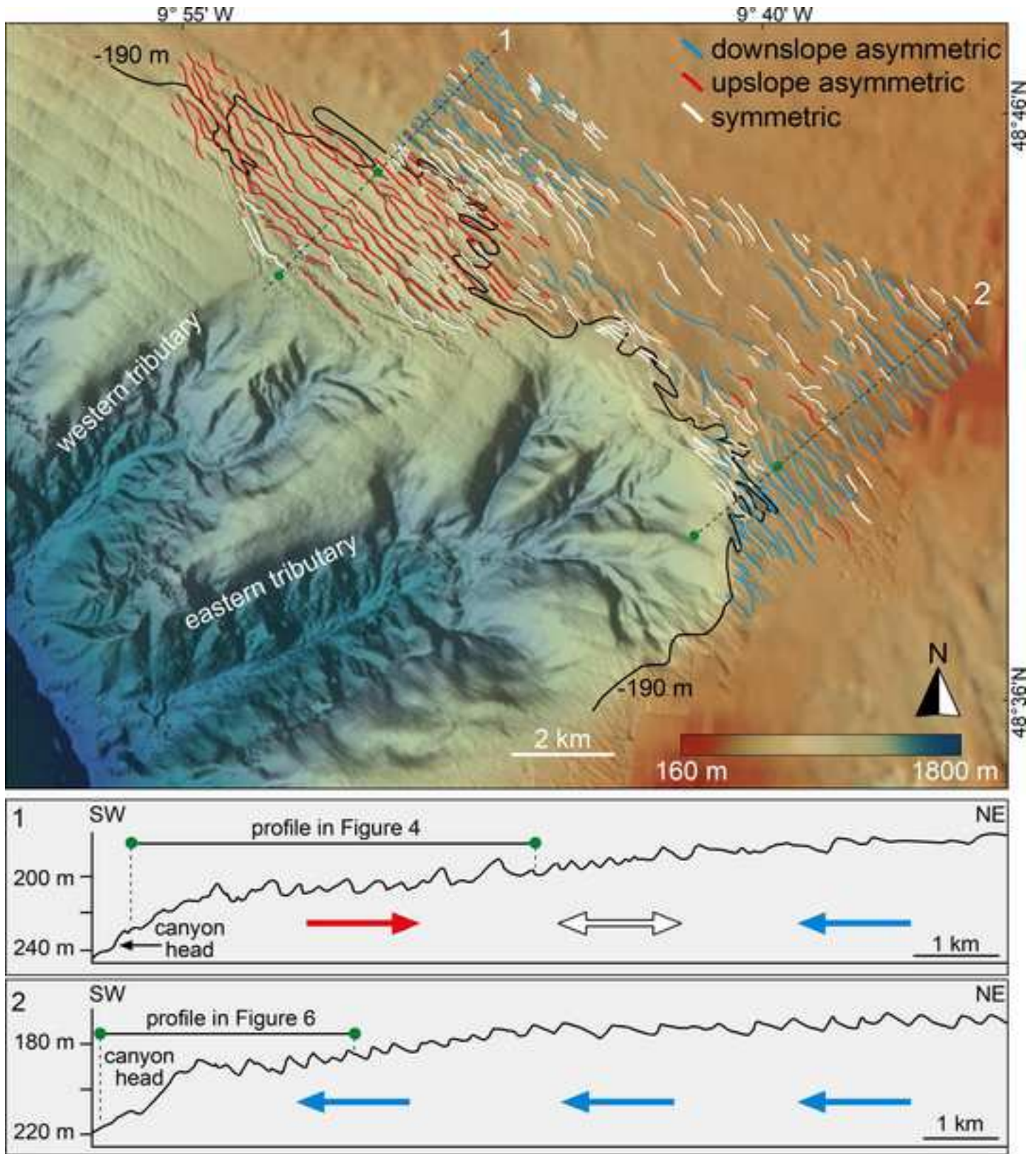


Fig.3 - Lo lacono et al., 2019

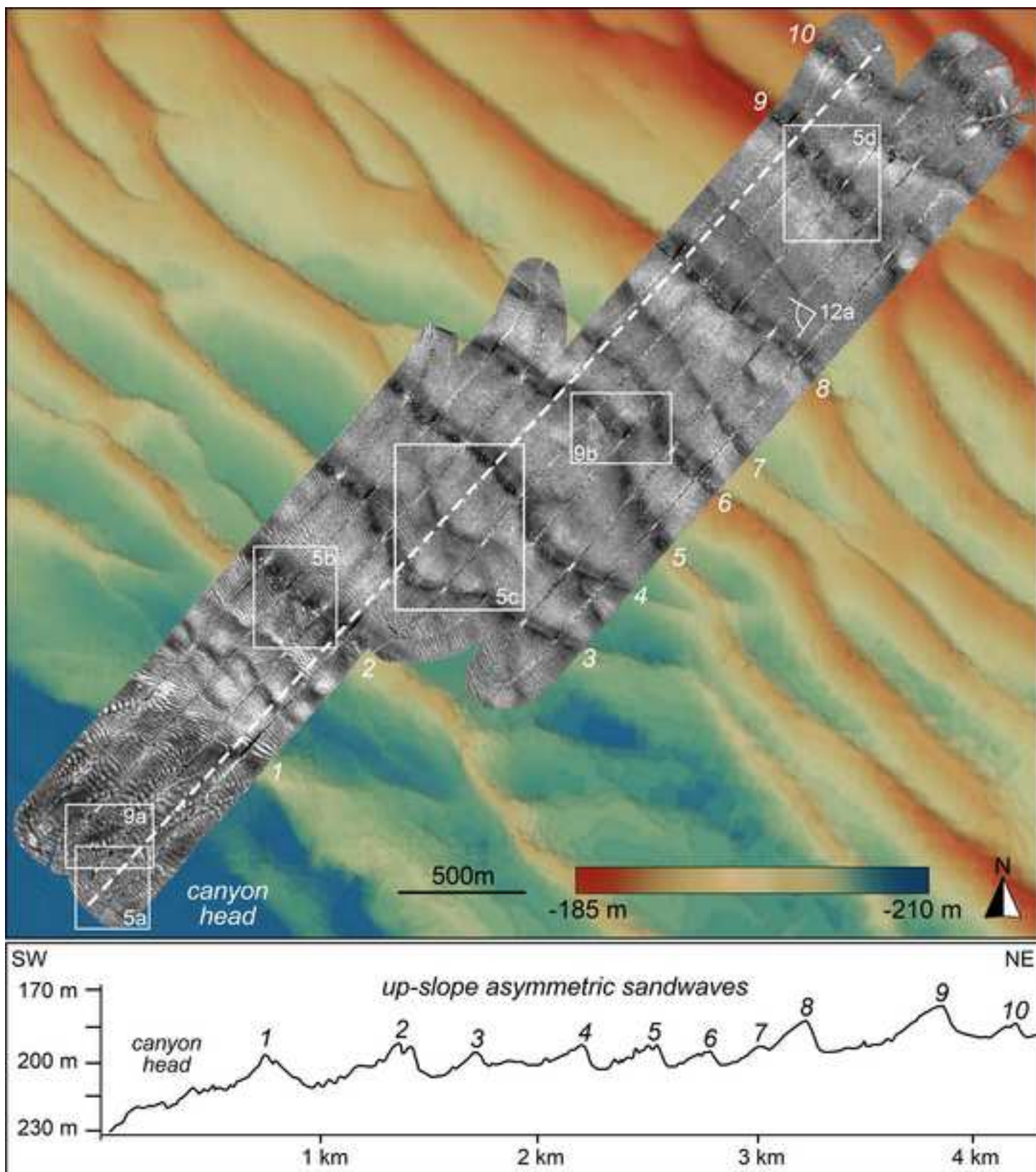


Fig.4 - Lo lacono et al., 2019

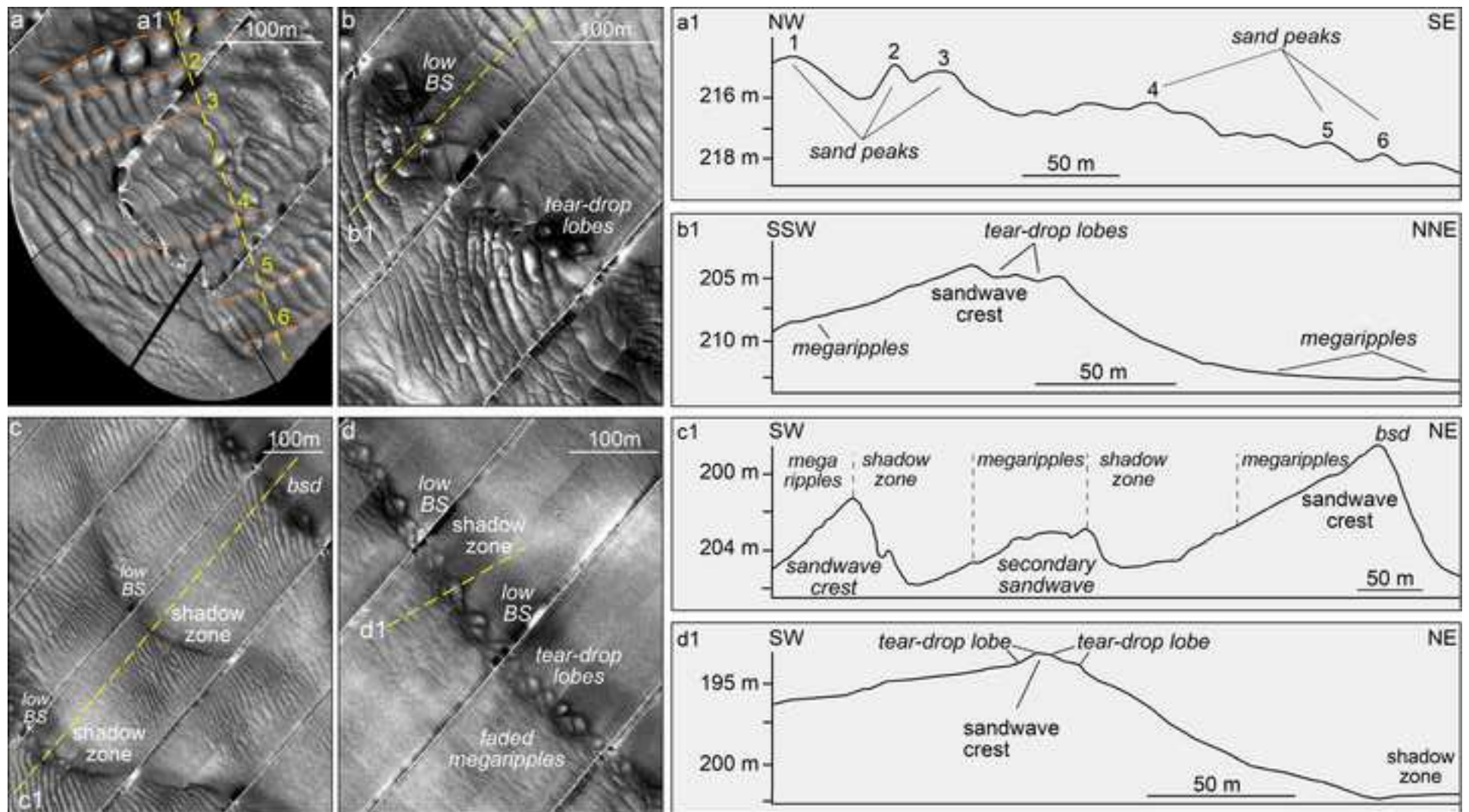


Fig.5 - Lo lacono et al., 2019

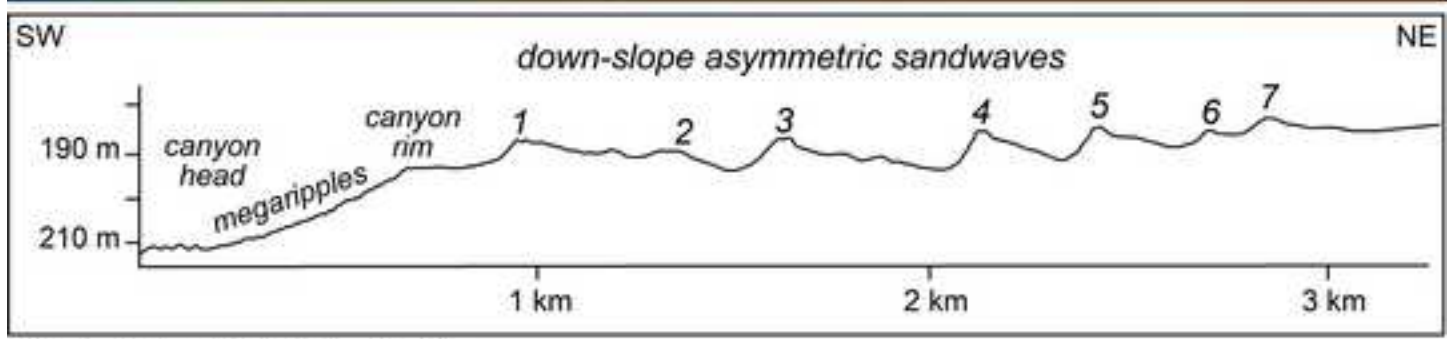
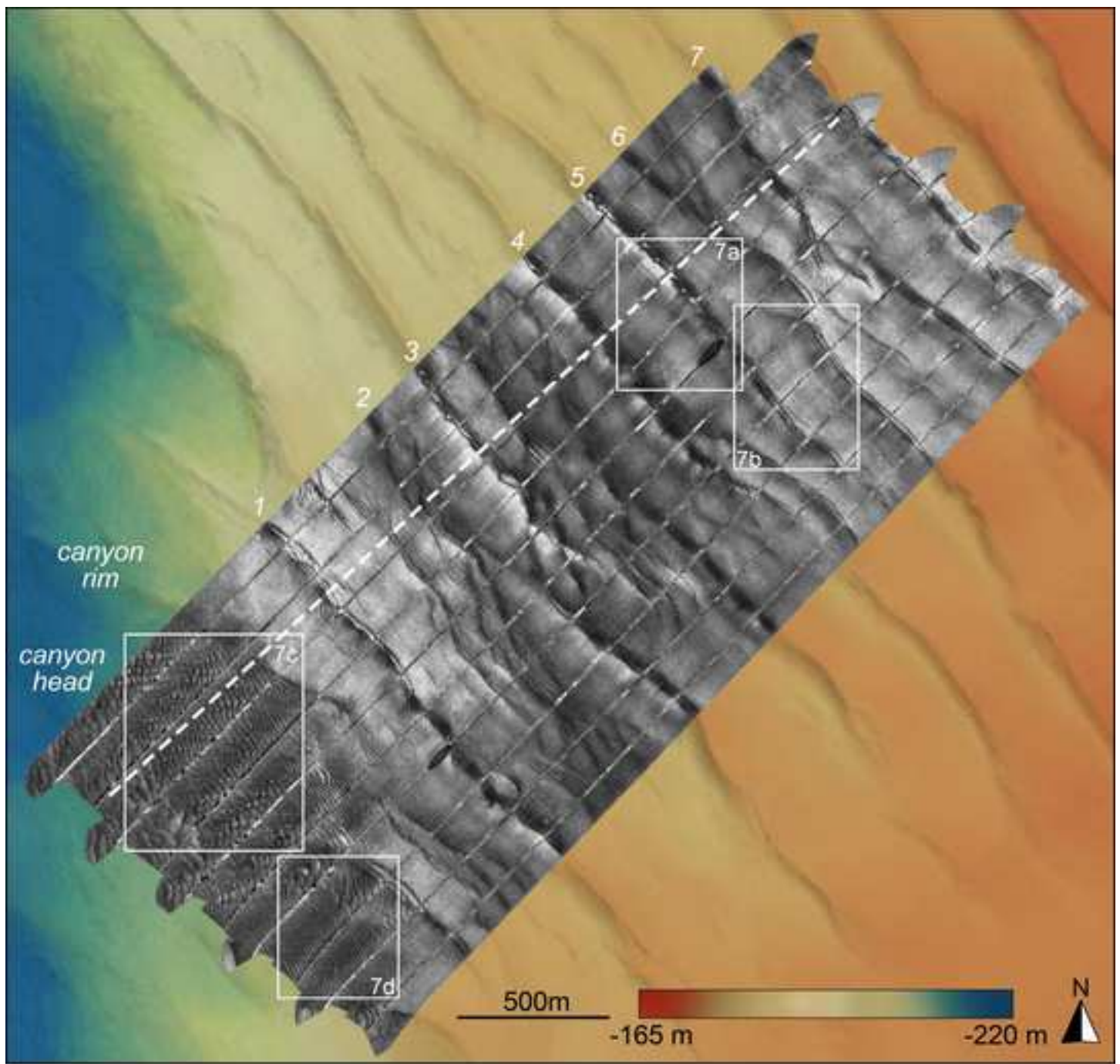


Fig.6 - Lo lacono et al., 2019

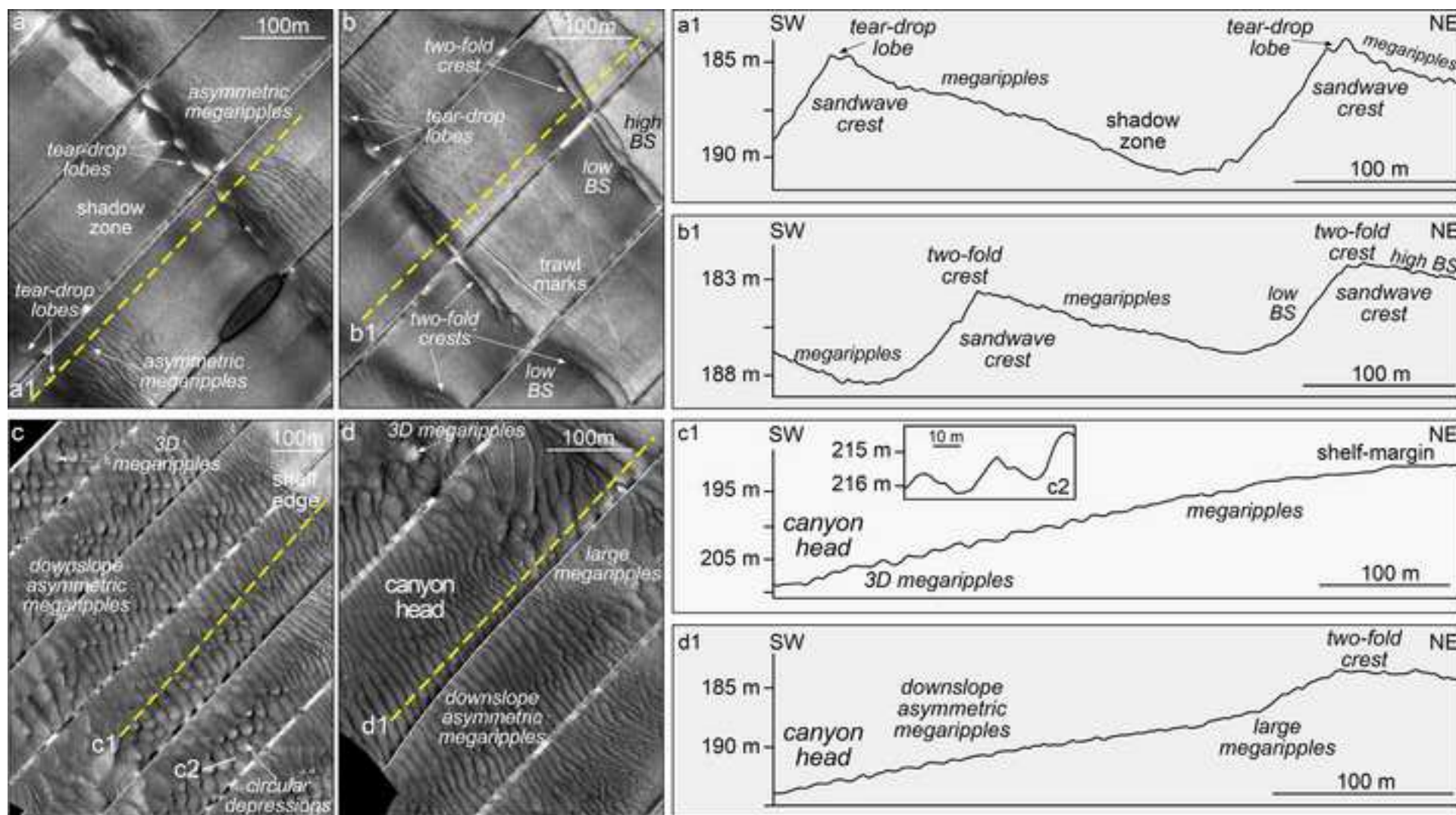


Fig.7 - Lo Iacono et al., 2019

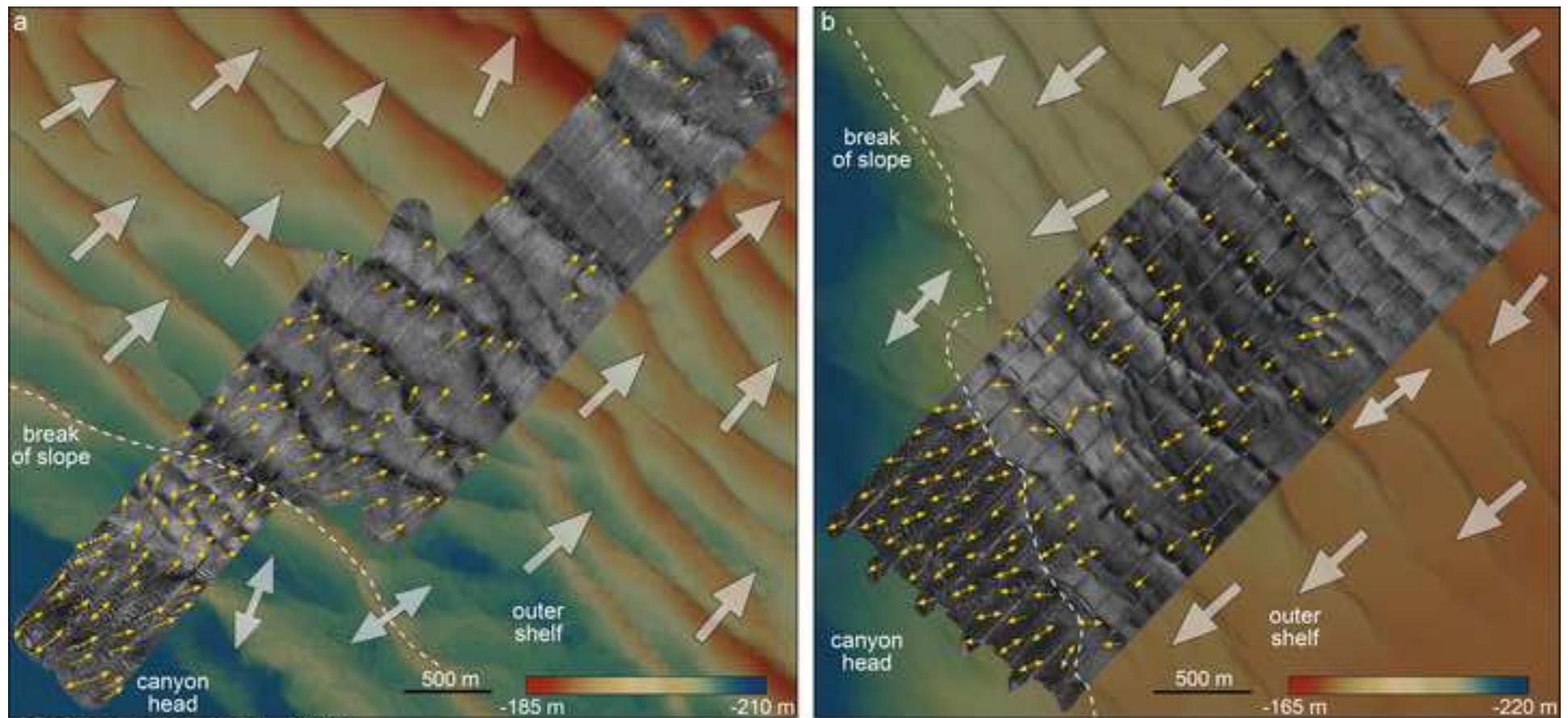


Fig.8 - Lo lacono et al., 2019

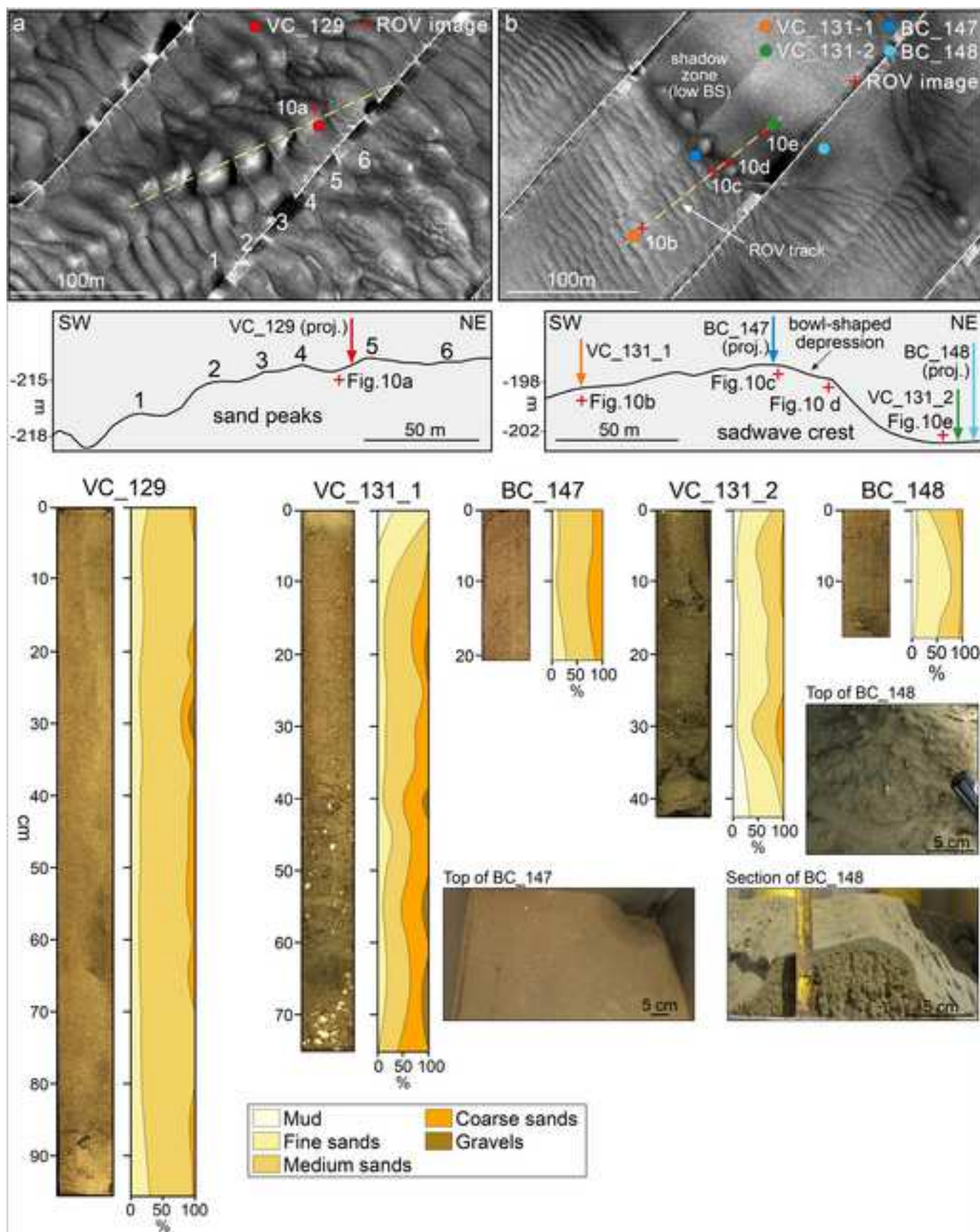


Fig.9 - Lo lacono et al., 2019

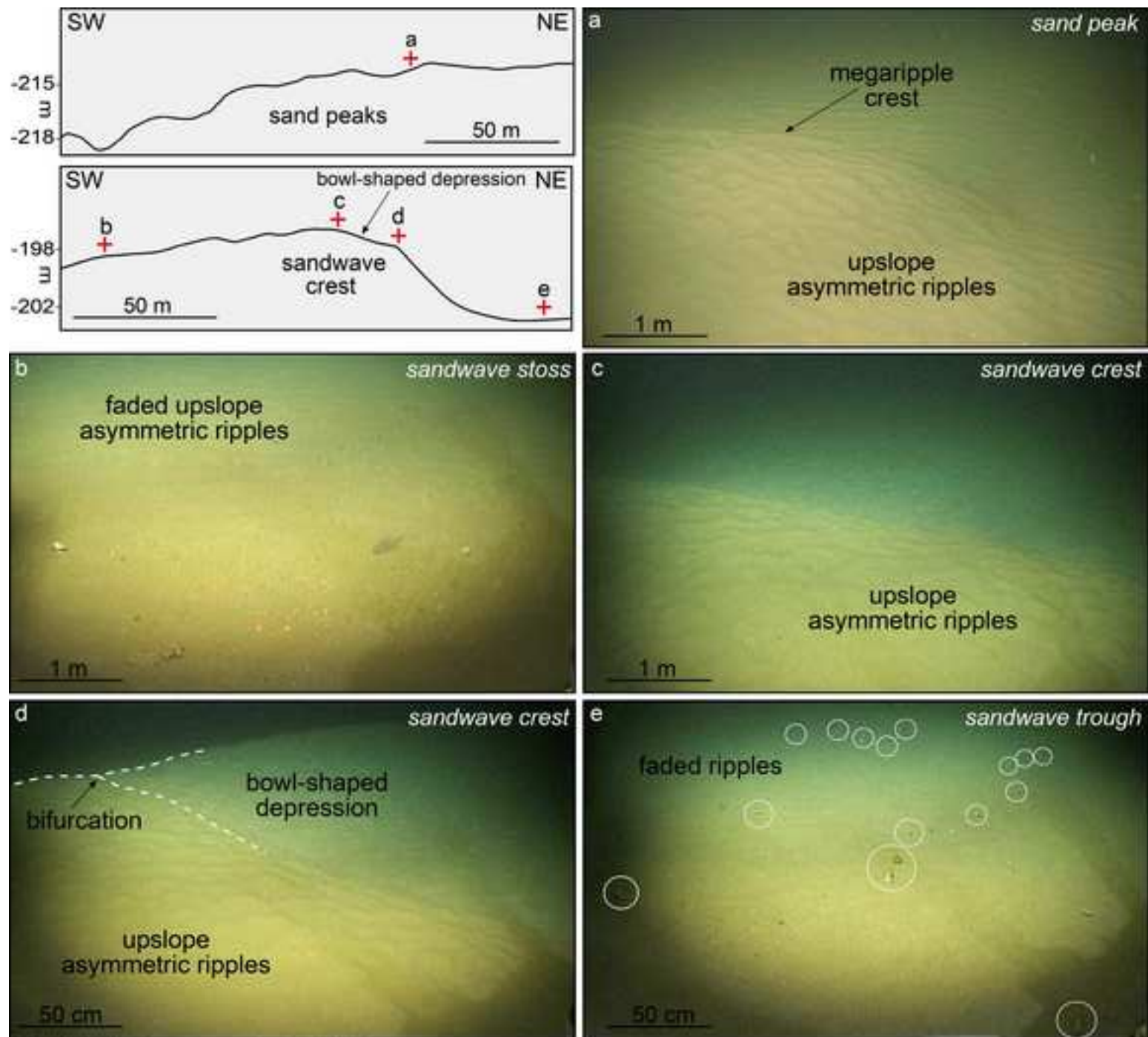


Fig.10 - Lo lacono et al., 2019

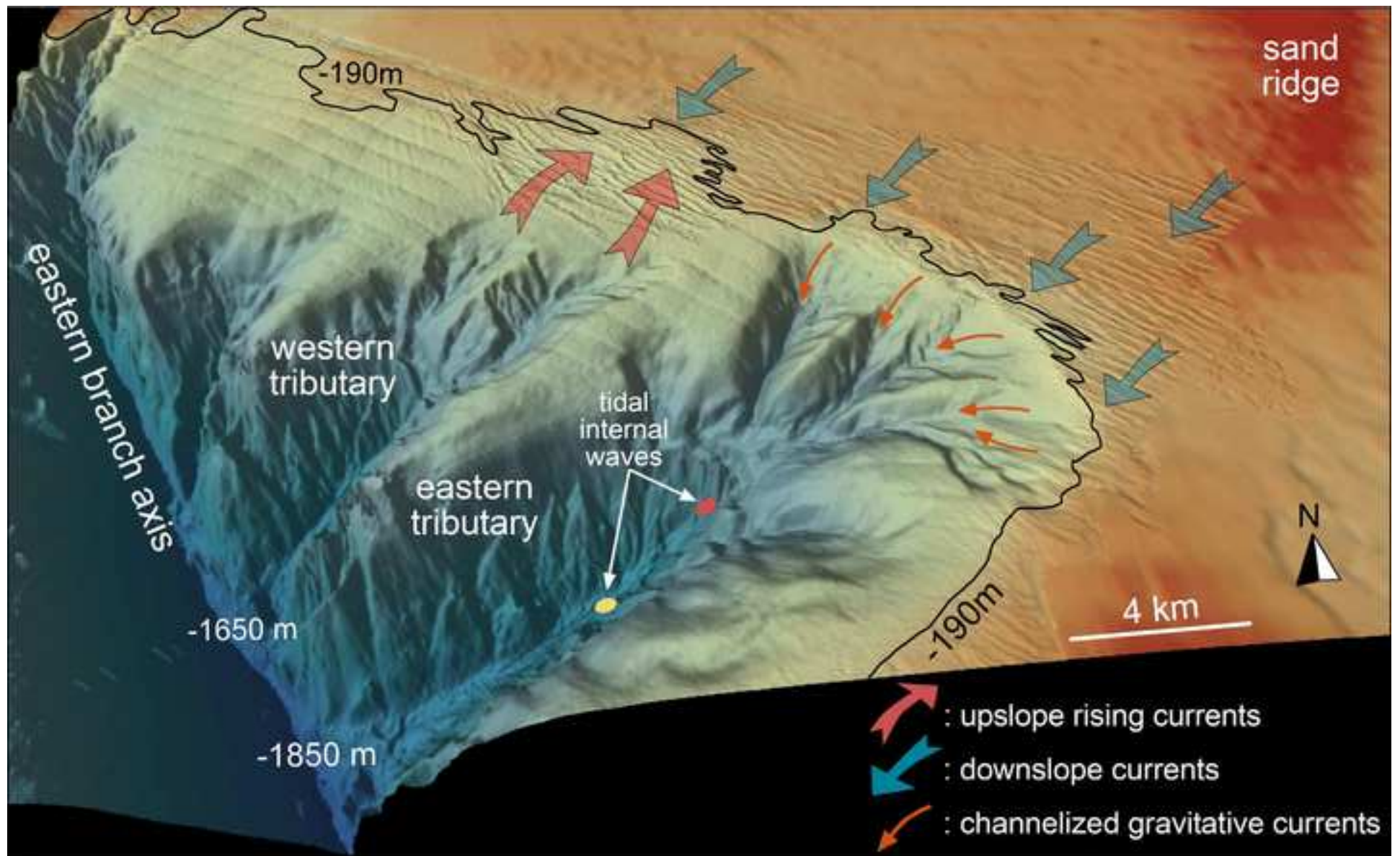


Fig.11 - Lo lacono et al., 2019

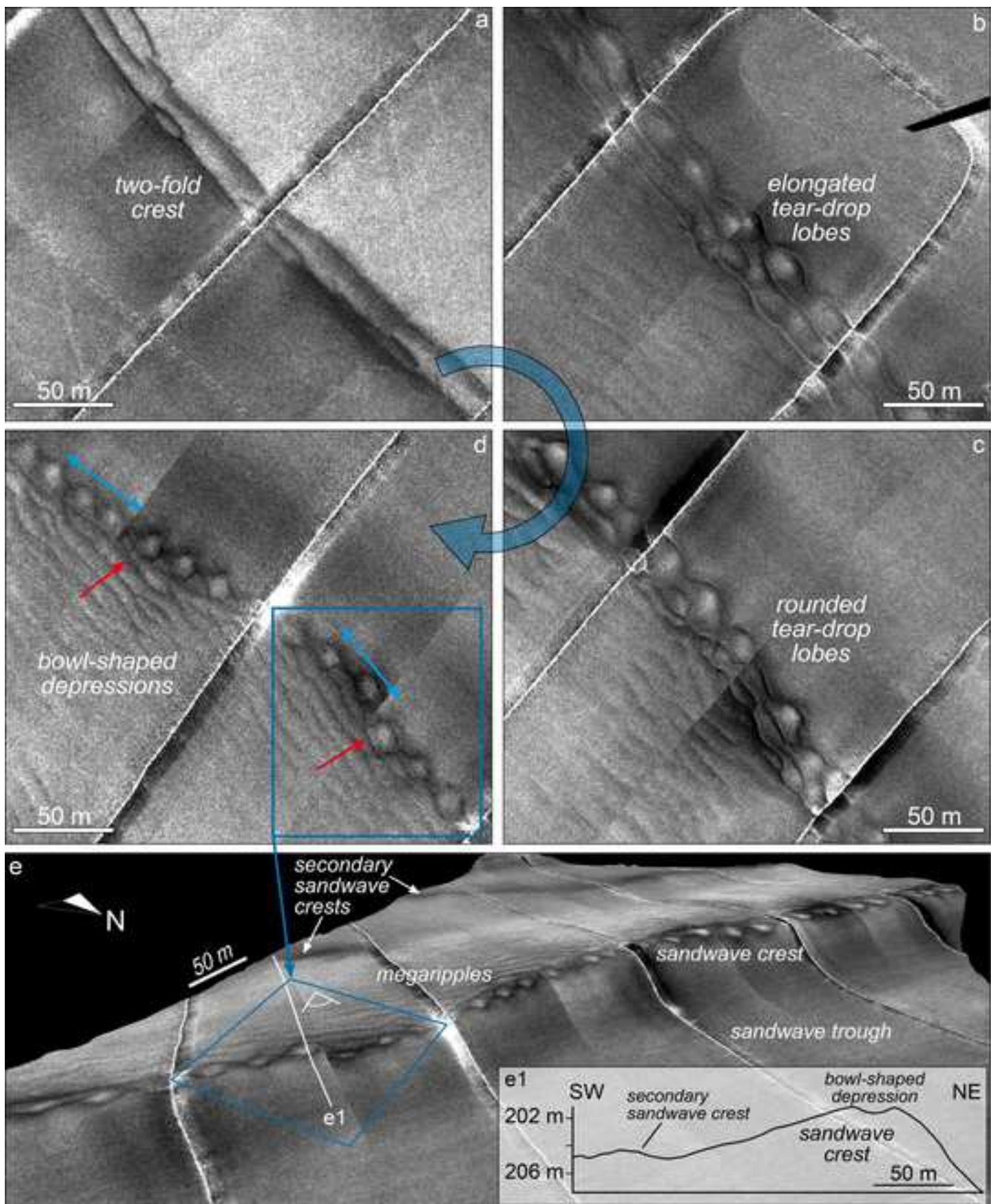


Fig.12 - Lo lacono et al., 2019